CHALMERS
UNIVERSITY OF TECHNOLOGY

Spatially-resolved characterization of the flow structure in a bubbling fluidized bed with solids crossflow

Powder Technology 482 (2026) 122620

Contents lists available at ScienceDirect

Powder Technology

journal homepage: www.journals.elsevier.com/powder-technology

Spatially-resolved characterization of the flow structure in a bubbling fluidized bed with solids crossflow☆

Munavara Farha [a,*], Henrik Ström [b], Diana Carolina Guío-Pérez [a], David Pallarès [a]

[a] Division of Energy Technology, Chalmers University of Technology, SE-412 96 Gothenburg, Sweden
[b] Division of Fluid Dynamics, Chalmers University of Technology, SE-412 96 Gothenburg, Sweden

HIGHLIGHTS

- Eulerian–Eulerian CFD approach is used to study solids transport mechanisms in bubbling beds with crossflow.
- Low crossflow produces stable, counter-rotating vortex structures in the bed.
- High crossflow disrupts vortex coherence, raising macro-dispersion of solids.
- Increased bed height produces larger vortex macrostructures and higher solids dispersion.
- Bubble- and cluster-induced mixing is two orders of magnitude higher than random motion.

GRAPHICAL ABSTRACT

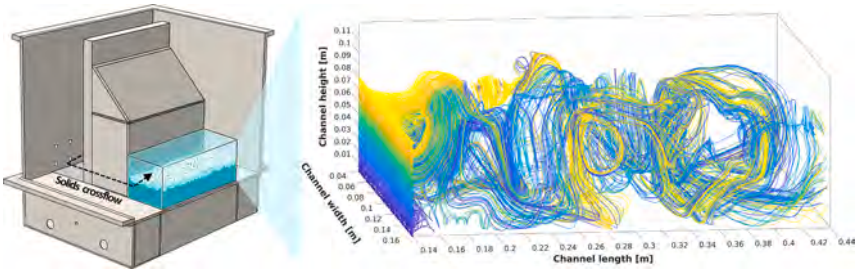

ARTICLE INFO

Keywords:
Fluidization
Bubbling fluidized bed
Fluid-dynamical scaling
Solids mixing
Solids crossflow
Eulerian-Eulerian CFD model

ABSTRACT

The aim of this study is to characterize the flow structure in a bubbling fluidized bed with a horizontal solids crossflow. Such configurations are integral to the processes of chemical looping combustion, indirect gasification, drying, and coating, where solids mixing and precise control of the solids residence time distribution are critical for maximizing reactor efficiency and/or product quality. This work combines Eulerian-Eulerian computational fluid dynamics (CFD) modeling with experiments in a fluid-dynamically down-scaled cold-flow model. The experiments provide a physical basis for assessing the reliability of the numerical predictions, while the CFD analysis delivers detailed spatial and temporal characterization of flow phenomena not directly accessible via measurement. The closed-loop unit incorporates a module that induces convection of the solids crossflow along a horizontal transport channel, which has an up-scaled cross-sectional width of 0.92 m and a loop length of 10.35 m. The unit is designed and operated according to Glicksman's simplified scaling laws to replicate industrial conditions for thermochemical processes that involve bubbling fluidization, specifically, a bed of sand-like particles (density, 2650 kg/m^3; mean diameter, 950 μm) operated at 800 °C. In this setup, two operational parameters are varied: the bed height (0.67–0.83 m at settled state); and the solids crossflow rate (yielding mean solids velocities in the range of 0–0.15 m/s).

The CFD model is validated against measurements of the bed voidage, solids velocity, and solids dispersion coefficient. Thereafter, the simulated data are analyzed along the horizontal flow direction, so as to provide high-resolution insights into the local distributions of convective (solids velocity) and dispersive (turbulent kinetic energy) solids transport. The results indicate that at low crossflow rates (yielding $Pe \approx 0.03$–0.64), the solids flow is dominated by the formation of counter-rotating vortical structures, resulting in substantial regions within

☆ This article is part of a Special issue entitled: 'FBC25' published in Powder Technology.

* Corresponding author.
E-mail address: m.farha@chalmers.se (M. Farha).

https://doi.org/10.1016/j.powtec.2026.122620
Received 30 October 2025; Received in revised form 22 April 2026; Accepted 28 April 2026
Available online 5 May 2026

which solids move in the direction opposite to the crossflow. At high crossflow rates (yielding $Pe \approx 1.29–4.52$), the vortical flow structures are largely disrupted, resulting in flow patterns in which the particle trajectories are more elongated and less streamlined, with only a small fraction of the solids exhibiting reverse flow. Importantly, macroscopic dispersion increases due to the longer and less-streamlined paths that the particles follow. Analysis of dispersion at the micro-scale reveals that the turbulent component, driven by bubble and cluster motions, is two orders of magnitude greater than the laminar counterpart associated with random particle motion and collisions. Vertical dispersion peaks at mid-height in the dense bed, whereas horizontal dispersion is highest near the gas distributor and at the bed surface. These observations indicate that bubble and wake formation, as well as bubble bursting, are the primary mechanisms driving the horizontal mixing of solids in bubbling fluidized beds.

1. Introduction

Bubbling fluidized beds with solids crossflow are used across many industries because they provide efficient gas-solid contacts, high thermal mixing, and capacity for handling high flowrates of solids. In thermochemical processes, such as indirect pyrolysis/gasification and chemical looping combustion, solids crossflow arises from the circulation of solids that is required to ensure sufficient transport of heat and reactive materials between reactors [1–3]. In the chemical, pharmaceutical and food industries, crossflow configurations are adopted for throughput operations such as drying, coating, and granulation, where controlling the particle residence time distribution (RTD) and uniform exposure to process conditions is essential for high product quality [4–6]. In the iron reduction industry, the gas-solids crossflow arrangement allows for optimization of the chemical potential driving the heterogeneous reaction [7]. Regardless of the application, a comprehensive mechanistic understanding of the solids flow is essential for the effective design, scale-up, and optimization of these systems.

The gas-solids hydrodynamics of fluidized beds have been extensively studied, as they strongly influence mass and heat transfer and reaction rates, which in turn impact overall process efficiency [8–10]. A flow pattern analysis typically involves examining the spatial development of the solids velocity profile and quantifying solids mixing [1,10–14]. This characterization yields insights into residence time distribution, recirculation patterns, and potential flow issues such as dead zones and bypassing [11,15]. Although advanced measurement techniques, e.g., radioactive particle tracking [16], magnetic particle tracking [17], positron emission particle tracking [10], X-ray tomography [18], and electrical capacitance tomography [19] provide valuable spatial and temporal insights into solids flow patterns, experimental constraints limit their ability to resolve fully the flow structures in gas-solids systems.

Computational fluid dynamics (CFD) address these limitations by providing data at a spatial resolution that is unattainable through experiments alone. Previous CFD-based studies have investigated the complex flow structures and solids circulation patterns characteristic of fluidized bed systems. For instance, Li and Kuipers, using a discrete particle simulation (DPS) approach, analyzed the gas-solids flows in fluidized beds, showing that bubble formation, particle collisions, and local heterogeneities significantly affect the distribution and mixing of solids [20]. Cooper and Coronella demonstrated that solids circulate through bubble wakes that transport particles from the distributor to the surface [21]. Lateral exchange between the wake and bulk phase was also identified as a dominant mechanism influencing the flow structure. Similarly, Norouzi et al. [16] applied the CFD-Discrete Element Method (DEM) model to resolve solids circulation by tracking individual particle trajectories, explicitly identifying gross circulation loops spanning the bed height and internal circulation at the bubble scale. Their results showed that particle entrainment in bubble wakes governs axial solids transport, while wake-induced lateral displacement contributes to radial mixing. Sun et al. [22], applying the Eulerian-Eulerian model with granular kinetic theory, linked turbulent particle motion and energy spectra to inhomogeneous flow fields and intensified wall-region fluctuations. Distinct circulation patterns have also been reported. Luo et al. [23] identified a double-recirculation pattern, entailing central particle ascent and wall-side descent, which revealed structured loops driven by bubble activity. Askarishahi et al. [24] observed four dominant vortices, with solids rising near the walls and descending centrally at lower heights, together with reversal at the top, indicating vortex-induced circulation. Bakshi et al. [25] used fine-grid, two-fluid simulations to show that gas bypass (throughflow) and bubble-induced wake interactions drive complex, inhomogeneous flow fields that critically influence solids redistribution. Xie et al. [26] examined the influence of boiler geometry using CFD-DEM, showing that bubble growth, rupture, and lateral expansion shape distinct circulation regimes.

Bubbling fluidized beds with significant solids crossflows have been investigated in a limited number of studies. Sette et al. [27] applied potential flow theory to describe the solids velocity field in a cold-flow model of an industrial indirect gasifier, showing that crossflow-driven convection acts in concert with bubble-induced dispersion. Farha et al. [28], using magnetic tracer measurements, characterized the horizontal solids transport in a bubbling fluidized bed with crossflow, and applied three modeling approaches (deconvolution, convection-dispersion, and compartment modeling) to interpret the residence time distributions. They found that the dispersion coefficient scales linearly with the crossflow rate, and that increasing the crossflow rate, bed height, or fluidization velocity reduces the extent of the dead zones, thereby improving fluidization quality. Zhang et al. [29] analyzed solids flow in a horizontal fluidized bed dryer with a screw conveyor by conducting tracer-based RTD experiments and fitting the results with dispersion and tanks-in-series models, showing that higher screw rotation rates promoted plug flow and reduced back-mixing. Koleilat et al. [30] demonstrated that inclined distributor jets generate a toroidal flow field in a fluidized bed granulator, and, using dense flow tracking of video imaging, showed that the angular velocity of this circulation increases with higher air jet velocity and decreases with greater bed mass, directly correlating toroidal flow intensity with enhanced mixing of bed solids.

System compartmentalization has also been investigated in terms of its impacts on controlling large-scale mixing and improving operational stability. Kong et al. [31] assessed the solids mixing in a shallow crossflow bubbling fluidized bed (with/without baffles) by measuring the RTD in tracer experiments and testing multiple compartment models, finding that the plug-flow-with-dispersion model best described the system. In the absence of baffles, gas maldistribution caused the solids in the upper bed layers to follow preferential paths across the channel, bypassing the dense phase and producing non-uniform transport. With baffles, this bypass was suppressed as solids were redistributed into the dense region, resulting in a more-coherent solids convection that was strongly influenced by the gas velocity and bed length, although only weakly by bed height. Using electrical capacitance tomography and pressure mapping, Migliozzi et al. [32] observed that the flow of bubbles and the dense emulsion phase are controlled by the gas distribution between compartments and the design of the inter-compartmental wall openings. Uneven fluidization promoted asymmetric exchange between compartments and destabilized the interfaces, with solids transfer found to be highly sensitive to the configuration of the walls and fluidization rates. Esence et al. [33] employed a compartment model calibrated with tracer experiments to analyze

particle RTD in a shallow crossflow fluidized-bed solar reactor, showing that compartmentalization narrowed the RTD and reduced backmixing, with higher compartment numbers and fluidization rates further enhancing solids flow uniformity.

Recent studies have employed advanced CFD simulations, often in combination with targeted experiments, to elucidate how specific design and operating parameters shape both global and local solids flows. Hua et al. [34] analyzed solids RTD in a dense fluidized bed with crossflow and with continuous solids feeding, combining cold-flow experiments with Eulerian-Eulerian CFD simulations. At higher fluidization velocities, the solids followed more-direct cross-channel paths with reduced backmixing, producing a plug-flow-like pattern and narrower RTDs. In contrast, higher rates of solids feeding intensified the recirculation loops in the dense phase, broadening the RTD toward well-mixed conditions. The addition of baffles disrupted the large-scale recirculation loops, reduced lateral dispersion, and thereby promoted more-uniform solids transport. Zou et al. [35] examined the RTD in a multi-compartment fluidized bed using a Eulerian-Eulerian CFD model. They demonstrated that dividing the bed into compartments using internal baffles transformed the flow pattern to being closer to plug flow, thereby reducing backmixing. Increasing the gas velocity or outlet height led to broader RTDs, due to greater fluidization heterogeneity and faster particle exit, while double internal circulations improved flow uniformity and extended the residence time by mitigating bypassing. Geng et al. [36] analyzed the solids RTD in a crossflow bubbling fluidized bed using a Eulerian-Eulerian CFD model, finding that a higher solids inventory promoted broader RTDs, whereas a higher solids flux resulted in a narrower RTD. In all cases, the tail of the RTD curves followed an exponential decay, reflecting delayed particle exiting, caused by internal recirculation within the dense phase. Zou et al. [37] simulated the solids RTD in bubbling fluidized beds using Eulerian-Eulerian CFD model with a structure-based drag formulation. Increasing the solids feed rate promoted plug-flow behavior, whereas increasing the fluidization velocity or bed height broadened the RTD, enhanced bubbling heterogeneity, broadened the distributions, and promoted stronger backmixing. Furthermore, the velocity profiles revealed a core-annulus pattern with upwards solids motion in the central region and downwards return flow near the walls, while the gas crossflow drove the particles sideways across the channel. Parvathaneni et al. [38] performed Eulerian simulations of gas-solid fluidized beds to study bubbling and jetting regimes under different gas injection modes. Their results showed that the injection configuration strongly affects the formation and evolution of flow structures, including jet penetration, jet breakage, and bubble formation. As the superficial gas velocity increases, jets merge and form larger bubbles, which enhances particle circulation and mixing within the bed.

Vollmari and Kruggel-Emden [39] analyzed the RTD in a dual-chamber fluidized bed using a CFD-DEM approach validated with ultra-high frequency RFID tracking. The results of that study showed that a higher solids mass inflow reduced the mean residence time and narrowed the RTD, as frequent particle entry displaced the existing material and accelerated turnover. In contrast, a higher fluidization velocity expanded the bed and promoted particle passage over the inter-chamber weir, thereby shortening the residence time but broadening the RTD. Two distinct mechanisms of cross-chamber transfer were identified: particle passage under the wall driven by pressure differences; and particle passage over the wall mediated by bubble-induced splashing. Jia et al. [40] conducted CFD-DEM simulations of fluidized beds with wide PSDs to investigate the interaction between bubble behavior and particle mixing. The results showed that bubbles act as a driving force for particle mixing by generating annular-core flow structures. Furthermore, in the partially fluidized regime, both bubble size and the bed mixing index increased with increasing superficial gas velocity. Kazemi et al. [41] investigated particle mixing in a bubbling fluidized bed using a CFD-DEM approach. The results showed that the mixing index increased with particle granular temperature and bubble size, indicating that stronger particle velocity fluctuations and larger bubbles enhance particle mixing within the bed.

Collectively, the cited studies show that the solids crossflow in fluidized beds results from a complex interplay between convection (linked to the solids flowrate) and dispersion (linked to mixing). Although some previous works have provided spatial resolution, the flow structures and governing hydrodynamic mechanisms remain insufficiently explored; the novelty of the present study lies in delivering a comprehensive mechanistic mapping of the mixing patterns and flow structures observed in such configurations, including their formation and disruption. The aim of the present study is to explore how the presence of a crossflow influences the solids flow structures and transport mechanisms in bubbling fluidized beds. Specifically, the objectives are to characterize solids convection and dispersion, to examine their interplay, and to assess how operational parameters (bed height and solids-conveying velocity) influence the flow structures and mechanisms governing solids transport. Accordingly, the study employs scaled cold-flow experiments to validate the spatially-resolved analysis provided by Eulerian-Eulerian CFD simulations. The experimental unit is operated with Geldart B-type solids, and Glicksman's simplified scaling laws are applied to replicate the hydrodynamics of hot, large-scale operation.

2. Theory

2.1. Fluid-dynamic scaling

Fluid-dynamic downscaling enables the investigation of large gas-solid systems, typically operating at high temperatures and/or high pressures, and often in harsh atmospheres, by replicating their fluid-dynamic behaviors in less-complex models under ambient conditions. These cold-flow models offer increased flexibility, allow the use of advanced diagnostics, and ensure improvement in both safety and cost-efficiency. In this study, Glicksman's simplified set of scaling laws is applied, preserving key dimensionless numbers across the full-scale hot unit and the downscaled model [42,43]:

$$\frac{u_0^2}{gD_b}, \frac{\rho_s}{\rho_g}, \frac{u_0}{u_{mf}}, \frac{G_s}{\rho_s u_0}, \frac{L_1}{L_2}, \varphi, PSD$$

Glicksman's simplified scaling laws, which have been extensively validated in experimental studies [43–45], modify the original formulation by replacing the particle and unit Reynolds numbers with the ratio of superficial to minimum fluidization velocity $[u_0/u_{mf}]$. This substitution allows greater flexibility in length scaling, as it depends on the ratio of the minimum fluidization velocities, i.e., for the specific gas-solids pair, as derived from the manipulation of the *Fr*-numbers shown in Eq. (1):

$$[L] = \frac{\left[\frac{u_{mf}^2}{g \cdot Fr}\right]_{cold}}{\left[\frac{u_{mf}^2}{g \cdot Fr}\right]_{hot}} = \left(\frac{[u_{mf}]_{cold}}{[u_{mf}]_{hot}}\right)^2 \quad (1)$$

2.2. Gas-solids multiphase model

In this study, the gas-solids flow is modeled using the Eulerian-Eulerian approach, in which both phases are treated as interpenetrating continua [46–50]. Balance equations for mass and momentum are solved for both the gas and solids phases, with interphase momentum exchange terms accounting for their interactions. The behavior of the solid phase is described using the kinetic theory of granular flow (KTGF) [13,46,51]. Table 1 summarizes the governing equations and constitutive relations used in the present model.

Table 1
Governing equations and constitutive relations employed in the present framework.

Conservation of mass equations:	
$\frac{\partial}{\partial t}\left(\varepsilon_g\rho_g\right)+\nabla\cdot\left(\varepsilon_g\rho_g\vec{u}_g\right)=0$	[2]
$\frac{\partial}{\partial t}\left(\varepsilon_s\rho_s\right)+\nabla\cdot\left(\varepsilon_s\rho_s\vec{u}_s\right)=0$	[3]
Momentum balance equations:	
$\frac{\partial}{\partial t}\left(\varepsilon_g\rho_g\vec{u}_g\right)+\nabla\cdot\left(\varepsilon_g\rho_g\vec{u}_g\vec{u}_g\right)=-\varepsilon_g\nabla P+\nabla\cdot\bar{\bar{\tau}}_g+\varepsilon_g\rho_g\vec{g}-\beta_{gs}\left(\vec{u}_g-\vec{u}_s\right)$	[4]
$\frac{\partial}{\partial t}\left(\varepsilon_s\rho_s\vec{u}_s\right)+\nabla\cdot\left(\varepsilon_s\rho_s\vec{u}_s\vec{u}_s\right)=-\varepsilon_s\nabla P-\nabla P_s+\nabla\cdot\bar{\bar{\tau}}_s+\varepsilon_s\rho_s\vec{g}+\beta_{gs}\left(\vec{u}_g-\vec{u}_s\right)$	[5]
Granular kinetic energy transport equation:	
$\frac{3}{2}\varepsilon_s\rho_s\left[\frac{\partial\theta_s}{\partial t}+\vec{u}_s\nabla\cdot\theta_s\right]=\bar{\bar{\tau}}_s:\nabla\vec{u}_s+\nabla\cdot\left(\kappa_{\theta_s}\nabla\theta_s\right)-\gamma_{\theta_s}$	[6]
Constitutive equations:	
Gas-phase stress tensor:	$\bar{\bar{\tau}}_g=-\varepsilon_g\left[\left(\xi_g-\frac{2}{3}\mu_g\right)\left(\nabla\cdot\vec{u}_g\right)I+\mu_g\left(\nabla\vec{u}_g+\left(\nabla\vec{u}_g\right)^T\right)\right]$ [7]
Solids-phase stress tensor:	$\bar{\bar{\tau}}_s=-\varepsilon_s\left[\left(\xi_s-\frac{2}{3}\mu_s\right)\left(\nabla\cdot\vec{u}_s\right)I+\mu_s\left(\nabla\vec{u}_s+\left(\nabla\vec{u}_s\right)^T\right)\right]$ [8]
Inter-phase momentum exchange coefficient [46,52–54]:	$\beta_{gs}=\frac{3}{4}C_D\frac{\varepsilon_s\varepsilon_g\rho_g\left\lvert\vec{u}_g-\vec{u}_s\right\rvert}{d_p}\varepsilon_g^{-2.65},\quad$ for $\varepsilon_g>0.8$ [9]
	$C_D=\begin{cases}\frac{24}{\varepsilon_g Re_s}\left[1+0.15\left(\varepsilon_g Re_s\right)^{0.687}\right], & Re_s<1000\\ 0.44, & Re_s>1000\end{cases}$ [10]
	$\beta_{gs}=150\frac{\varepsilon_s^2\mu_g}{\varepsilon_g d_p^2}+1.75\frac{\varepsilon_s\rho_g\left\lvert\vec{u}_g-\vec{u}_s\right\rvert}{d_p},\quad$ for $\varepsilon_g\le0.8$ [11]
Solids shear viscosity [55]:	$\mu_s=\mu_{s,c}+\mu_{s,k}+\mu_{s,f}$ [12]
Collisional viscosity [54]:	$\mu_{s,c}=\left[\frac{4}{5}\varepsilon_s\rho_s d_p g_0(1+e)\left(\frac{\theta_s}{\pi}\right)^{\frac{1}{2}}\right]$ [13]
Kinetic viscosity [56]:	$\mu_{s,k}=\left[\frac{\rho_s d_p\sqrt{\theta_s\pi}}{6(3-e)}\left(1+\frac{2}{5}(1+e)(3e-1)\varepsilon_s g_0\right)\right]$ [14]
Frictional viscosity [53]:	$\mu_{s,f}=\left[\frac{P_s\sin\varphi_f}{2\sqrt{I_{2D}}}\right]$ [15]
Solids bulk viscosity [46,54]:	$\xi_s=\frac{4}{3}\varepsilon_s^2\rho_s d_p g_0(1+e)\left(\frac{\theta_s}{\pi}\right)^{\frac{1}{2}}$ [16]
Solids pressure [46,54]:	$P_s=\rho_s\varepsilon_s\theta_s\left[1+2(1+e)g_0\varepsilon_s\right]$ [17]
Radial distribution function [13,46,54]:	$g_0=\left[1-\left(\frac{\varepsilon_s}{\varepsilon_{s,max}}\right)^{\frac{1}{3}}\right]^{-1}$ [18]
Granular conductivity [54,57]:	$\kappa_{\theta_s}=\frac{150\rho_s d_p\sqrt{\theta_s\pi}}{384(1+e)g_0}\left[1+\frac{6}{5}\varepsilon_s g_0(1+e)\right]^2+2\rho_s\varepsilon_s^2 d_p(1+e)g_0\sqrt{\frac{\theta_s}{\pi}}$ [19]
Collision energy dissipation [53]:	$\gamma_{\theta_s}=\frac{12(1-e^2)g_0}{d_p\sqrt{\pi}}\rho_s\varepsilon_s^2\sqrt{\theta_s^3}$ [20]

2.3. Solids transport mechanisms

Solids mixing in stationary bubbling fluidized beds is governed by particle-bubble dynamics. In the dense bed, the solids phase undergoes a downward drift as the particles move to fill the voids created by the rising bubbles [1,58]. Simultaneously, particles from the emulsion surrounding the bubbles are entrained into the bubble wake and lifted upwards by the bubbles [1,58]. In the splash region, bubble eruptions at the bed surface eject solids in a ballistic manner, propelling the particles laterally [1,58]. This interplay of vertical and lateral transport forms generates a toroidal solids circulation pattern around preferential bubble paths, with the solids rising in the bubble wakes and descending between bubbles [59–61]. As illustrated in Fig. 1, the introduction of a horizontal solids crossflow superimposes an additional convective field onto the flow, resulting in a macroscopic net solids transport that is additional to the dispersive (mixing) component generated by the bubble flow. Thus, macroscopic convection refers to the bulk, mean horizontal movement of particles that results from the imposed crossflow [10,11], while macroscopic dispersion describes the mixing of particles in this mean flow, arising from both localized velocity fluctuations (due to collisions and small-scale turbulence) and the above-described, larger-scale motions that are driven by bubble passages and coherent flow structures [10,62].

Dispersion characterizes the spreading of solids due to the stochastic movement of particles in the bed, analogous to Brownian motion in a homogeneous phase [17,59–61]. Dispersion in fluidized beds occurs on two distinct scales: macro and micro. Macro-scale dispersion arises from the cumulative effect of multiple bubble passages and the coherent flow structures that they generate, often taking the form of large-scale vortices in stationary fluidized beds (i.e., bubbling beds without a crossflow). In this work, macro-scale dispersion is determined from the mean squared displacement (MSD) of multiple particle pathlines tracked over time. These pathlines are obtained from CFD modeling data, as described in Section 3.2.2. Following the classical Einstein equation, the MSD is calculated from the ensemble of various trajectory segments, yielding [23,63,64]:

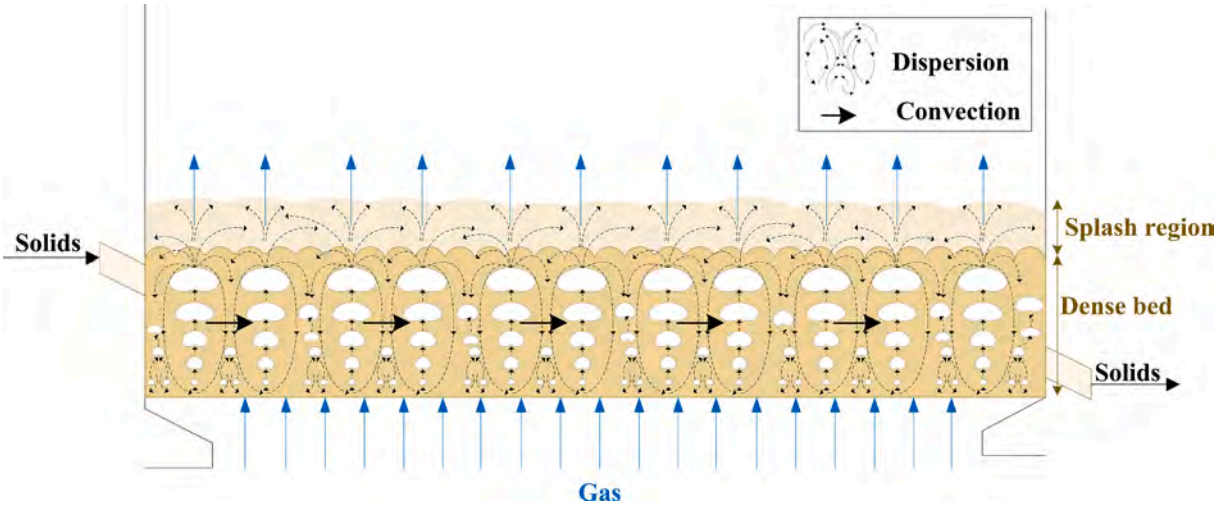

Fig. 1. Schematic of a bubbling fluidized bed with solids crossflow.

$$D_{macro,i} = \frac{\sum_{k=1}^{N} \varepsilon_{s,k} \cdot \frac{\left(\Delta r_{i,k}^{disp}\right)^2}{2\Delta t_k}}{\sum_{k=1}^{N} \varepsilon_{s,k}} \tag{21}$$

where $\Delta r_{i,k}^{disp}$ represents the dispersion-related particle displacement in direction i over the time interval Δt_k for the k-th trajectory segment. The summation weighs each pathline segment k according to the local solids volume fraction at its starting point, $\varepsilon_{s,k}$. Thus, the dispersion coefficient is obtained from half the slope of the linear region of the MSD-versus-time curve [10,65–67]. Note that if a macroscopic convection field characterized by a velocity field u_i is present (as in the case of solids crossflow), the dispersion-related particle displacement used in Eq. (21) becomes $\Delta r_{i,k}^{disp} = \Delta r_{i,k} - u_i \Delta t_k$.

Micro-scale dispersion encompasses both laminar and turbulent components. The laminar component arises from fluctuations in the velocities of individual particles around the local mean, primarily due to interparticle collisions [62,68–71]. An order-of-magnitude estimate of this quantity is obtained by dividing the granular temperature, i.e., the transported scalar in the kinetic energy conservation equation for solid particle fluctuations (see Eq. (6)), by the dominant fluctuation frequency [51,70–72]. Turbulent dispersion arises from the collective motion of bubbles and particle clusters, which generate eddies and promote localized mixing throughout the bed [13,62,68–71]. The intensities of these turbulent fluctuations can be quantified based on the time-averaged Reynolds normal stresses [13,54,68]:

$$\theta_{s,turbulent} = \frac{1}{3}\left\{\langle u'_{s,x}u'_{s,x}\rangle + \langle u'_{s,y}u'_{s,y}\rangle + \langle u'_{s,z}u'_{s,z}\rangle\right\} \tag{22}$$

where $u'_{s,i}$ denotes the fluctuating velocity component of the solid phase in the i-th direction ($i = x,y,z$).

The corresponding turbulent dispersion coefficient in the *i-th* direction is given by:

$$D_{turbulent,i} = \overline{u'_{s,i}u'_{s,i}}\tau_L \tag{23}$$

where τ_L represents the Lagrangian integral time scale, defined as:

$$\tau_L = \int_0^{\infty} \frac{\overline{u'_{s,i}(t)u'_{s,i}(t+t')}}{\overline{u'^2_{s,i}}} dt' \tag{24}$$

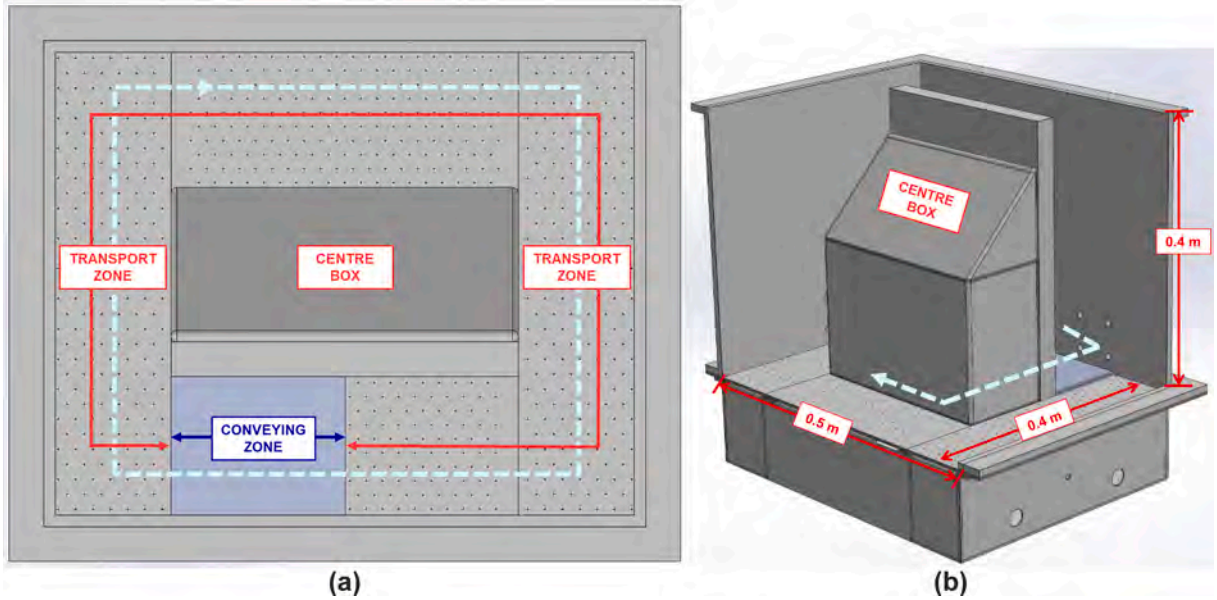

Fig. 2. Fluid-dynamically downscaled model with induced clockwise solids flow. (a) Top view. (b) Isometric view.

Table 2
Key parameters of the fluid-dynamically scaled model.

Parameter	Units	Hot unit	Cold model
Temperature	°C	800	24
Fluidization gas	–	Air or flue gases	Air
Gas density [ρ_g]	kg/m^3	0.359	1.187
Gas viscosity [μ_g]	kg/m•s	1.4×10^{-4}	1.54×10^{-5}
Bed geometry	m	L_{hot}	$0.12L_{hot}$
Bed material	–	Silica sand	Bronze
Particle density [ρ_p]	kg/m^3	2650	8770
Mean particle diameter [d_p]	μm	950	125
Gas superficial velocity [u_0]	m/s	u_{0hot}	$\sqrt{0.12}\, u_{0hot}$
Minimum fluidization velocity [u_{mf}]	m/s	0.31	0.074
Solids mean velocity [u_s]	m/s	u_{shot}	$\sqrt{0.12}\, u_{shot}$
Solids dispersion coefficient [D_s]	m^2/s	D_{shot}	$0.042D_{shot}$

This timescale represents the period during which velocity fluctuations remain correlated, indicating the persistence of turbulent motion [62,70–72].

3. Methodology

This section provides an overview of the methodology used to investigate solids transport in the present configuration. Section 3.1 describes the design and operation of the cold-flow model, including the scaling laws that were applied to replicate industrial conditions. Section 3.2 details the CFD model, covering the simulation settings, the selection of the analysis region (as only a specific portion of the system is analyzed), and the procedure for pathline tracking of the solids flow within this region.

Table 3
Summary of computational model parameters used.

Model parameter		Setting
Bed geometry dimension [3D]		0.5 m × 0.4 m × 0.5 m
Settled bed height [H]		0.08 m, 0.10 m
Bed inventory		63.5 kg, 79.3 kg
Mesh size		0.004 m
Mesh resolution [$\Delta x/d_p$]		10–20
Inlet boundary condition		Velocity
Outlet boundary condition		Pressure
Wall boundary condition		No slip
Velocity (superficial) inlet (transport zone) [u_{tz}]		0.23 m/s
Velocity (superficial) inlet (conveying zone) [u_{cz}]		0.26 m/s, 1.48 m/s
Solid material		Bronze
Particle diameter [d_p]		125 μm
Particle density [ρ_p]		8770 kg/m^3
Friction packing limit		0.61
Initial solids volume fraction [ε_s]		0.607
Maximum packing limit [$\varepsilon_{s,max}$]		0.63
Angle of internal friction [φ_f]		30°
Coefficient of restitution [e]		0.9
Gas		Air
Operating pressure		101,325 Pa
Pressure-velocity coupling		Phase-coupled SIMPLE
Spatial discretization method	Pressure	PRESTO!
	Momentum	Convective term: First-order upwind Diffusive term: Second-order accurate central differencing scheme
	Volume fraction	First-order upwind
Transient formulation		First-order implicit
Time step		10^{-5} s
Simulation time		30–40 s, depending on the condition tested

3.1. Cold flow model

The cold-flow model investigated in this study is shown in Fig. 2 and described in detail elsewhere [73]. The unit operates under bubbling conditions and is designed according to fluid-dynamic scaling laws to replicate large-scale, high-temperature operation (a bed of 950 μm silica sand fluidized with flue gas at 800 °C), with a length scaling factor of [L]=0.12. As illustrated in Fig. 2a, the unit features a closed-loop design in which a central box defines the main pathway for solids circulating around this box. The conveying zone, which is equipped with high-velocity nozzles and baffles, induces a steady, horizontal, clockwise circulation of the solids. In addition to the conveying zone, most of the loop consists of a fluidized channel, referred to as the 'transport zone', in which the conveyed solids flow horizontally. The unit has a footprint of 0.5 × 0.4 m and a height of 0.4 m. Both the conveying and transport zones are equipped with independently adjustable supplies of fluidization air. Table 2 compares the main parameters of the cold-flow model with those of its large-scale, high-temperature counterpart.

3.2. CFD model

3.2.1. Simulation setting

The 3D-CFD simulations were performed using the ANSYS Fluent software on 64 parallelized cores, requiring approximately 720 h to generate 30 s of simulation data. While such computationally intensive simulations are not suited for standard industrial workflows, they are essential for revealing the mechanisms behind observed trends, such as the positive correlation between solids velocity and dispersion coefficient in bubbling fluidized beds with crossflow (Farha et al. [28]); a trend that reduced-order models can capture and that has important implications for process optimization. The computational model parameters are summarized in Table 3. In this study, four cases are simulated by varying two operating parameters: the static bed height, H (0.08 m and 0.10 m); and the volumetric flowrate of air in the conveying zone, Q_{CZ} (2.58×10^{-3} m^3/s and 14.3×10^{-3} m^3/s).

In this study, the gas distributor plate (which is perforated) is represented in the simulations by a uniform velocity boundary condition at the inlet for computational simplicity; however, it is well documented that distributor design can significantly affect fluidization hydrodynamics. Jang et al. [74] found that the geometry of the gas distributor, particularly orifice size and pitch, directly influences bubble formation, with smaller and more closely spaced orifices generating smaller, more uniform bubbles. Nthatisi and Van Der Merwe [75] showed that the distributor's open area and pitch substantially affect pressure drops and bed expansion, and that poor distributor geometry can cause air maldistribution and dead zones. Gustafsson et al. [76] further demonstrated that a uniform (porous plate) gas inlet yields lateral solids dispersion coefficients approximately 2–4 times higher than those observed with a nozzle-type distributor. Therefore, in the present study, the use of a uniform velocity boundary condition may lead to an overestimation of lateral dispersion compared to what would be expected with the actual perforated distributor plate.

Recent computational studies have also highlighted the importance of accurately representing the particle size distribution (PSD) in fluidized bed simulations. Particle-resolved CFD-DEM approaches [77,78] implement PSD by assigning each simulated particle a diameter sampled from the target distribution, enabling direct modeling of mono-modal, Gaussian (typically $\sigma/d_{50}\approx0.2$), flat, or binary PSDs. In contrast, multi-fluid Eulerian models [79,80] discretize the PSD into several solid phases, each with a defined size and fractional volume, to approximate the experimental or desired distribution. The adopted PSDs in these works range from narrow ($\sigma/d_{50}\approx0.1$–0.2) to broad ($\sigma/d_{50}\geq0.3$), with wider distributions causing greater reductions in minimum fluidization velocity, enhanced segregation, and the development of heterogeneous clusters, leading to a more irregular bed microstructure. In the present study, the PSD (d_{10}-d_{50}-d_{90}=80–112-132 μm) yields a coefficient of

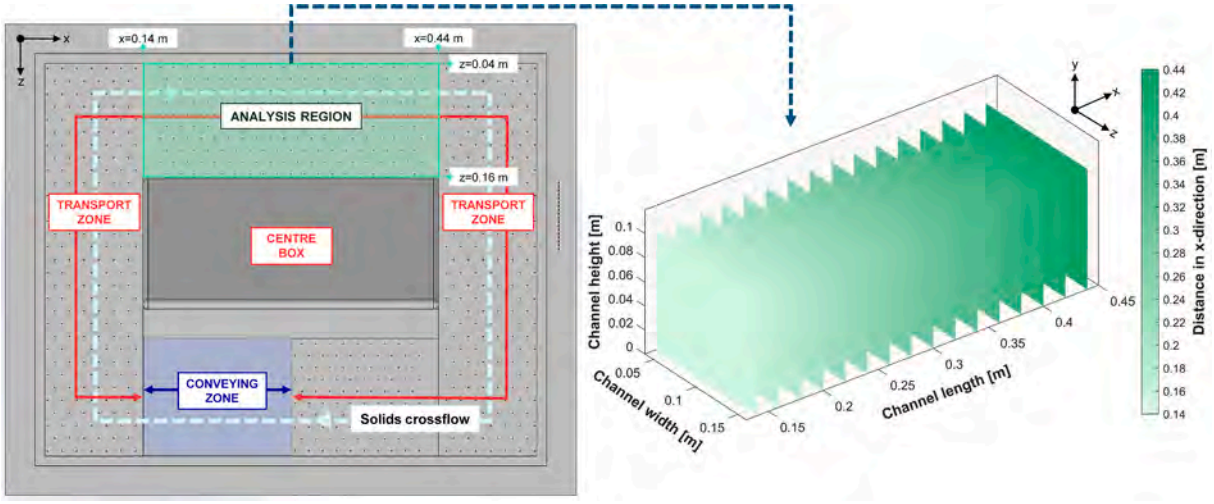

Fig. 3. Schematic of the cold flow model highlighting the analysis region (green) and data sampling planes along the *x*-direction. (For interpretation of the references to colour in this figure legend, the reader is referred to the web version of this article.)

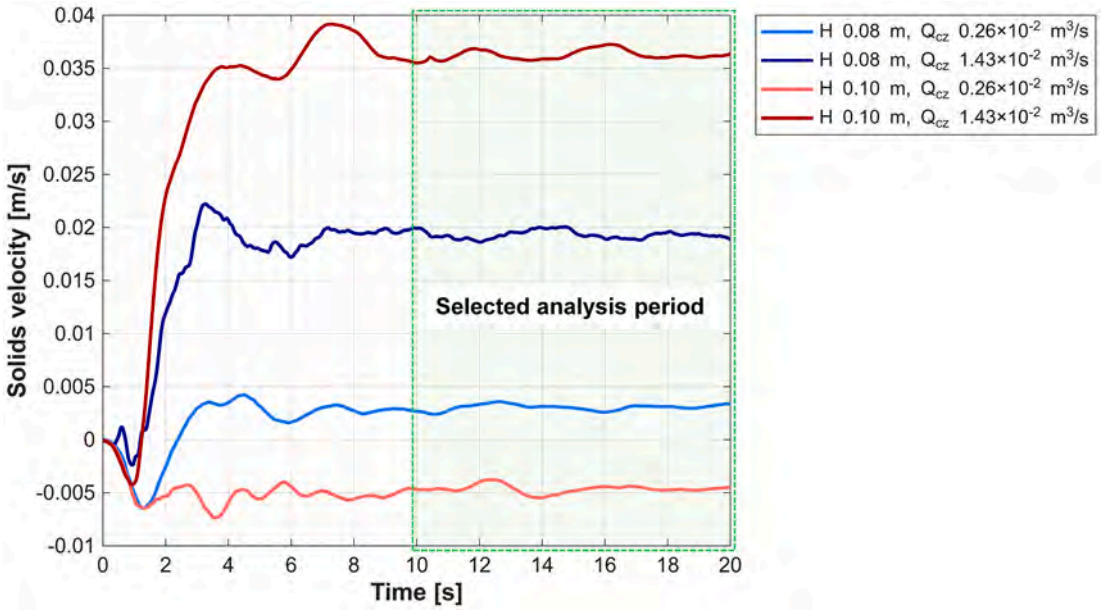

Fig. 4. Reverse time-averaged mass-weighted solids velocity in the direction of solids flow for each of the simulated conditions, illustrating the selection of the steady-state analysis window ($t \geq 10$ s).

variation (σ/d_{50}) of ~0.2, which is considered relatively narrow. Literature indicates that, at this level of polydispersity, representing the bed with the mean particle size is generally sufficient to capture the main fluidization behavior.

3.2.2. Analysis of simulated data

Although the entire 3D domain was modeled, the green-highlighted section in Fig. 3 was selected as the focus of this study, as it provides a relatively long straight channel and enables comparisons of model predictions with previous experimental data for validation (see Section 4). In this region, the net macroscopic solids convection occurs in the *x*-direction (x=0.14–0.44 m), while the channel width extends along the *z*-direction (z=0.04–0.16 m) and the bed height is defined along the *y*-direction, with y=0 corresponding to the gas distributor plate. Sixteen planes, oriented perpendicular to the solids flow direction and evenly spaced along the *x*-axis (Δx=0.02 m), were defined as reference locations for sampling the simulated data.

To study the solids flow pattern, particle pathlines were computed by numerically integrating the time-averaged simulated velocity fields. Trajectories were derived using a fourth-order Runge-Kutta (RK4) scheme [81]. The pathlines were initialized on a uniform grid within the physical bounds of the channel, oriented normal to the solids flow direction at the channel entry plane (x=0.14 m). These pathlines were also used to quantify the macro-dispersion of solids in the flow direction using the Einstein relation (see Eq. (21)). For these calculations, tracking was terminated when particles exited the region being analyzed.

4. Results and discussion

4.1. Identification of steady-state conditions

Before analyzing the simulation data, it is necessary to identify a time window that is representative of steady-state conditions. In this study, the steady state was determined by examining the temporal evolution of

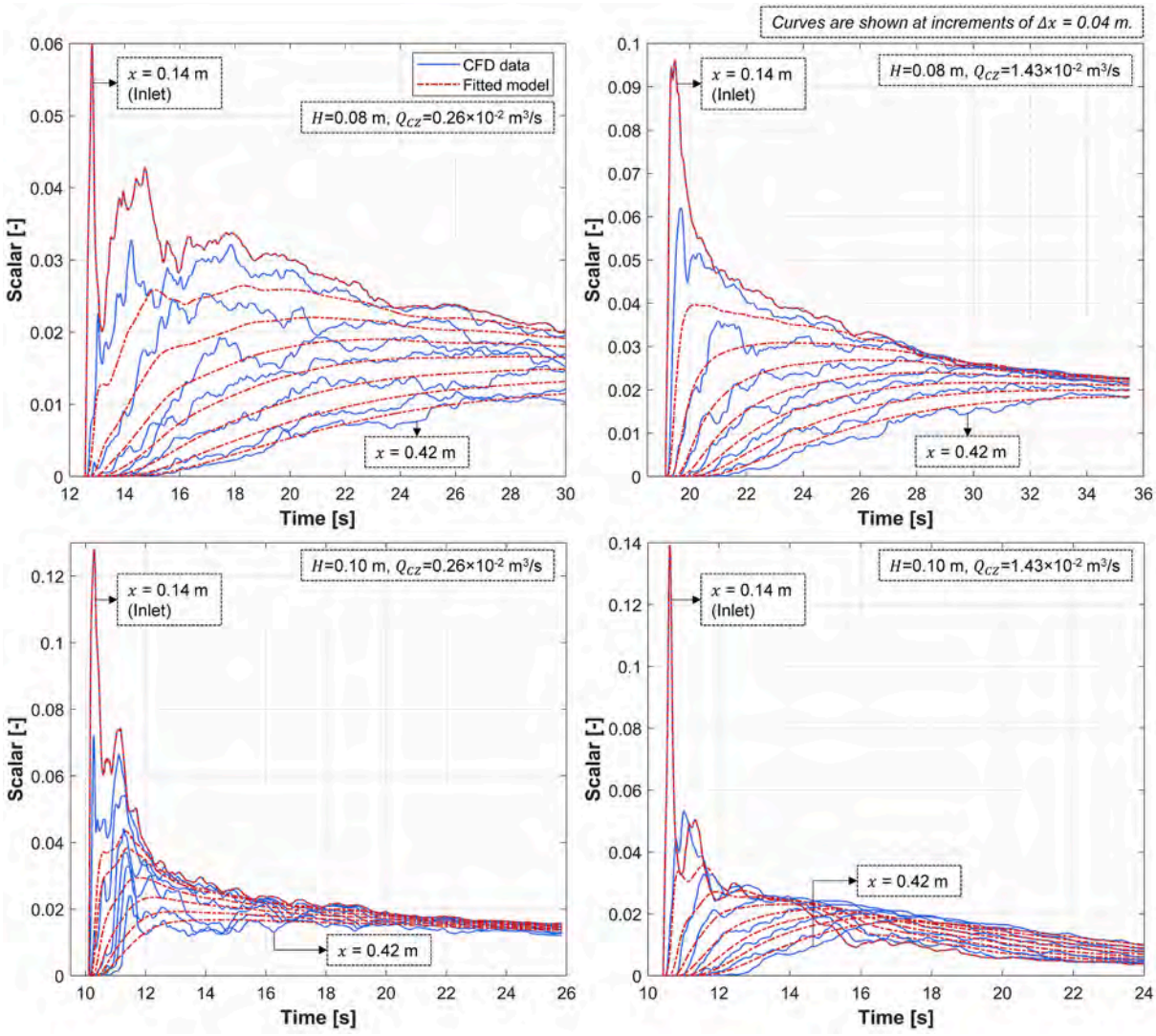

Fig. 5. Transient concentrations of a scalar tracer at various positions along the analysis region for the four tested conditions. CFD simulations (solid curves) versus fitted 1D convection-dispersion model results (dashed curves).

the solids velocity in the flow direction, using the mass-weighted average across the analysis region. Fig. 4 shows the reverse time-averaged value (i.e., averaged from a given time point to the end of the simulation) of the mean velocity for each of the four simulated conditions. This metric enables objective identification of the steady state, as it fluctuates during the initial transient period and stabilizes once the steady-state condition is attained. As shown in Fig. 4, the system typically reaches the steady state after approximately t=10 s in all cases. Consequently, a common analysis window of t=10–20 s was selected for all the simulations. The resulting 10 s datasets are considered statistically robust, as the bed's main frequency (estimated analytically according to [13,62]) is 3–4 Hz, which means that it captures approximately 30–40 cycles per sample.

4.2. Validation of the CFD simulation data

Once the time window ensuring steady-state conditions is identified, the fluid-dynamic validity of the simulation is assessed by comparing the CFD results with experimental measurements to verify that the key flow dynamics are captured. It should be noted that the CFD simulations in this work do not aim for exact replication of the experimental data but rather focus on achieving the same mixing regimes and flow structures for subsequent analysis. Therefore, no fine-tuning of the CFD model to

Table 4
Comparisons of the main parameters for overall solids transport, with data derived from CFD model and experiments. The ranges reported for the experimental data reflect the variability across multiple replicates.

Condition		Transport parameter	Experiment	CFD Model
H [m]	Q_{CZ} [m^3/s]			
0.08	2.58×10^{-3}	$u_{s,x}$ [m/s]	$(0.04 \pm 0.05) \times 10^{-3}$	0.64×10^{-3}
		$D_{s,x}$ [m^2/s]	$(1.01 \pm 0.01) \times 10^{-3}$	0.30×10^{-3}
0.08	14.3×10^{-3}	$u_{s,x}$ [m/s]	$(14.8 \pm 3.21) \times 10^{-3}$	7.76×10^{-3}
		$D_{s,x}$ [m^2/s]	$(2.03 \pm 0.41) \times 10^{-3}$	1.80×10^{-3}
0.10	2.58×10^{-3}	$u_{s,x}$ [m/s]	$(1.48 \pm 1.62) \times 10^{-3}$	0.19×10^{-3}
		$D_{s,x}$ [m^2/s]	$(1.77 \pm 0.07) \times 10^{-3}$	2.09×10^{-3}
0.10	14.3×10^{-3}	$u_{s,x}$ [m/s]	$(52.6 \pm 6.58) \times 10^{-3}$	52.31×10^{-3}
		$D_{s,x}$ [m^2/s]	$(3.31 \pm 0.27) \times 10^{-3}$	3.47×10^{-3}

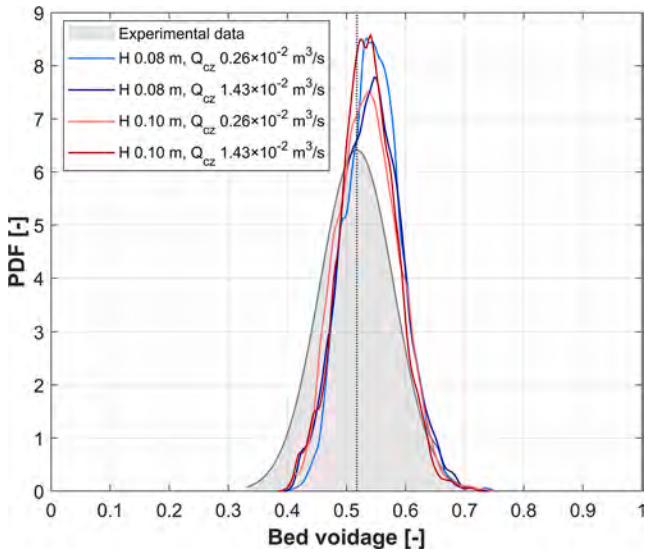

Fig. 6. Probability density functions of bed voidage for the four simulated conditions. The gray-shaded region indicates experimental data corresponding to the following condition: H=0.08 m; and Q_{cz}=1.03 × 10^{-2} m^3/s.

experimental measurements has been performed.

The first validation focused on solids transport dynamics by analyzing transient concentration profiles to determine solids velocity and dispersion coefficient. To quantify their relative contributions to the overall transport, the CFD simulations included the injection of a passive scalar, after the steady state was reached, into a 0.05 × 0.05 × 0.05 m^3 volume located 0.05 m upstream of the analysis region. This scalar, modeled as a non-reactive tracer with negligible diffusion, was advected by the simulated solids velocity field. Fig. 5 presents the resulting transient concentration of the scalar at multiple locations along the channel for all four tested conditions (solid lines). The figure also presents data (dashed curves) from a fitted 1D transient convection-dispersion model, in which the solids velocity ($u_{s,x}$) and dispersion coefficient ($D_{s,x}$) are used as fitting parameters. This fitted model uses the CFD-simulated concentration at the start of the analysis region as the inlet boundary condition, as detailed in [28].

Table 4 compares the solids velocity and dispersion coefficient values obtained by fitting a 1D convection-dispersion model to both the CFD simulation data and the experimental measurements from a previous study [28], under the same set of conditions. The CFD-derived values are in reasonable agreement with the experimental data, indicating that the simulations reliably capture the solids flow observed in the experiments. Both parameters are of similar order of magnitude, and the observed trends with respect to operating parameters are consistent. The four operational conditions tested span a broad range of Peclet numbers (Pe=0.03–4.57). The lowest crossflow condition serves as a reference stationary case due to the very low solids circulation rate.

Bed voidage is used as the second validation parameter, as it is highly sensitive to the closure expressions employed in the CFD simulations. Fig. 6 presents the probability density function (PDF) of the time-averaged bed voidage, ε_g, for all four simulated conditions. The data were sampled at 4 × 10^5 (simulations) and 60 (experiments) points across the analysis region indicated in Fig. 3. The gray-shaded distribution indicates values determined from pressure measurements (for details, see [73,82]) under the following conditions: H=0.08 m and Q_{cz}=1.03 × 10^{-2} m^3/s. It is evident that the CFD simulations are in good agreement with the experimental results, although they slightly over-predict the peak value (0.53–0.55, compared to the measured value of 0.52), serving as a validation of the model's ability to capture the characteristic gas-solids flow structure in the bed. As this study had the aim to use CFD data to analyze solids flow structures rather than to reproduce precisely the experimental results, the Gidaspow drag model [52,54] specified in Table *3* was used without additional tuning or calibration. As noted by Upadhyay et al. [83], closer agreement may be achieved by adjusting, for example, the drag model; however, this was not the objective of the present work.

4.3. *Analysis of the solids flow pattern*

This section examines the spatial distribution of solids transport within the analysis region indicated in Fig. 3. Section 4.3.1 analyzes spatial velocity profiles to identify local flow features and characterize the transition from recirculation-dominated to convection-dominated regimes. Section 4.3.2 investigates solids dispersion across micro- and macro-scales, distinguishing between laminar and turbulent contributions and assessing the impact of large-scale flow structures on overall particle dispersion.

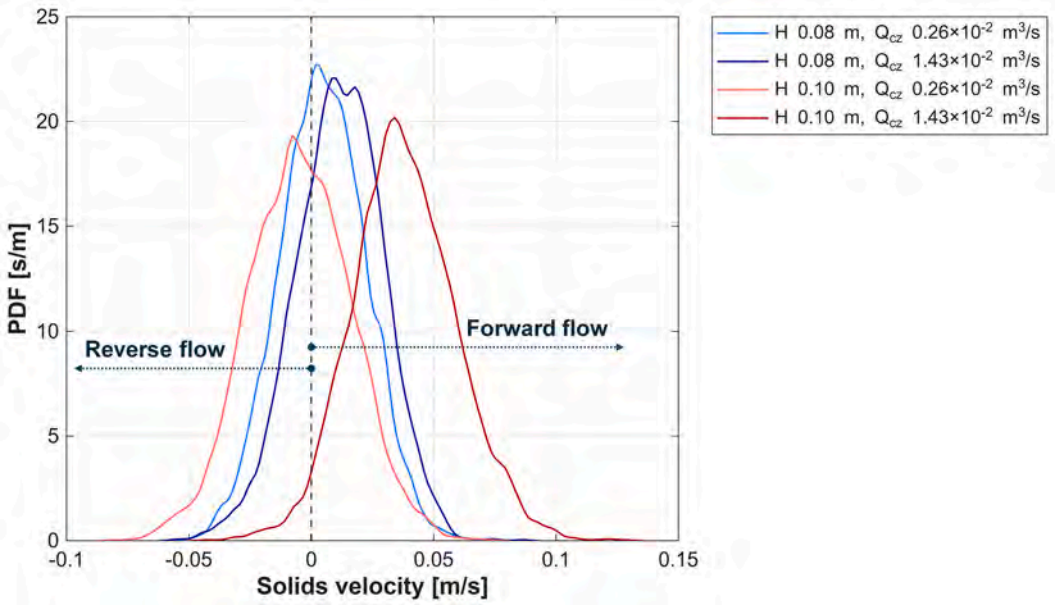

Fig. 7. Probability density functions of the solids velocities in the x-direction for the four simulated conditions.

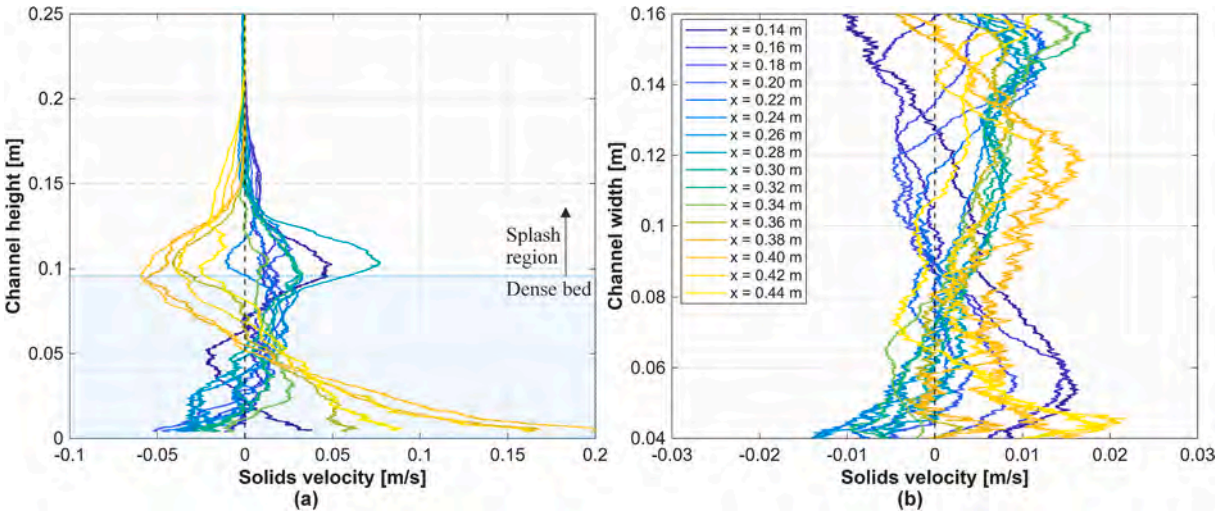

Fig. 8. Profiles of the solids velocities in the flow direction for different streamwise positions: (a) variation with channel height; (b) variation with channel width. Conditions: H=0.08 m; Q_{cz}=1.43 × 10^{-2} m^3/s. Note that the origin of the z-direction is defined such that the channel width extends from z=0.04 m to z=0.16 m.

4.3.1. Solids convection

Fig. 7 shows, for the four tested conditions, the statistical distribution of the x-component of the solids velocity, i.e., the one in the direction of the crossflow, averaged over the analysis region. The data reveals the presence of both forward and reverse flows of solids. Increasing the bed height and/or the fluidization flow rate in the conveying zone shifts the velocity distribution toward higher positive values, indicating enhanced net solids transport in the streamwise direction, which is consistent with previous observations [28,73] and the data in Table 4. The reverse flow fraction decreases from about 50% for the lowest crossflow conditions to less than 1% for the highest crossflow conditions, reflecting a clear transition from bidirectional transport to predominantly forward transport (see Appendix B). The Peclet number increases from Pe≈0.03–0.64 under low-flow conditions to 4.57 at the highest crossflow, indicating a shift toward convection-dominated transport in which the solids flow approaches a plug-flow pattern.

To interpret the above trends and connect the global velocity distributions to the underlying flow structures, we investigated the spatial variation of the solids velocity field. Fig. 8 presents the profiles of the solids velocity component in the crossflow direction at various streamwise positions: as a function of bed height (mass-weighted over the channel width, Fig. 8a) and as a function of channel width (mass-weighted over the bed height, Fig. 8b). The profiles shown correspond to the case with low bed height and high flowrate of conveying air. The vertical profiles (Fig. 8a) reveal a distinct evolution along the channel. In the upstream regions (x=0.14–0.28 m), forward flow dominates near the dense bed surface, while reverse flow is observed close to the distributor plate. Further downstream (x=0.34–0.44 m), this pattern is reversed, with reverse flow dominating near the bed surface and forward flow dominating adjacent to the distributor plate. Across all positions, high values for the streamwise velocity component are observed in proximity to the distributor plate and at the dense bed surface. The high velocities observed in the vicinity of the distributor plate are attributed to intense gas-solid interactions, wherein vertical gas jets and bubble formation give rise to the development of macrostructures within the system. These macrostructures subsequently alter the movement of solids along the streamwise direction, either promoting forward or backward motion depending on their spatial orientation. Close to the

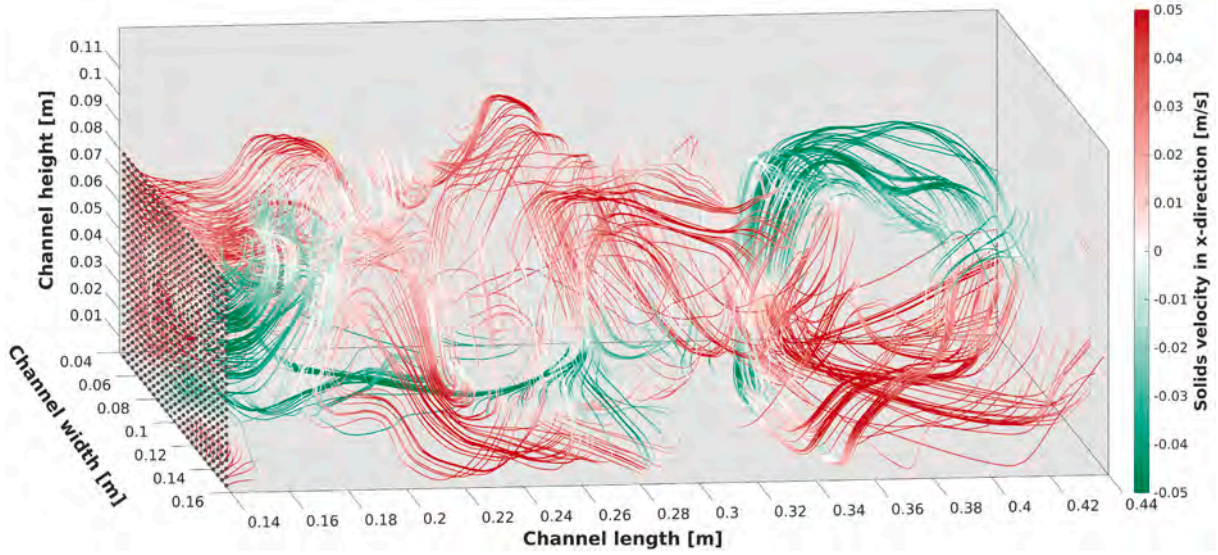

Fig. 9. Pathlines of the solids flow, showing organized recirculation patterns, with red and green segments indicating forward and reverse motions, respectively. Conditions: H=0.08 m; Q_{cz}=1.43 × 10^{-2} m^3/s. (For interpretation of the references to colour in this figure legend, the reader is referred to the web version of this article.)

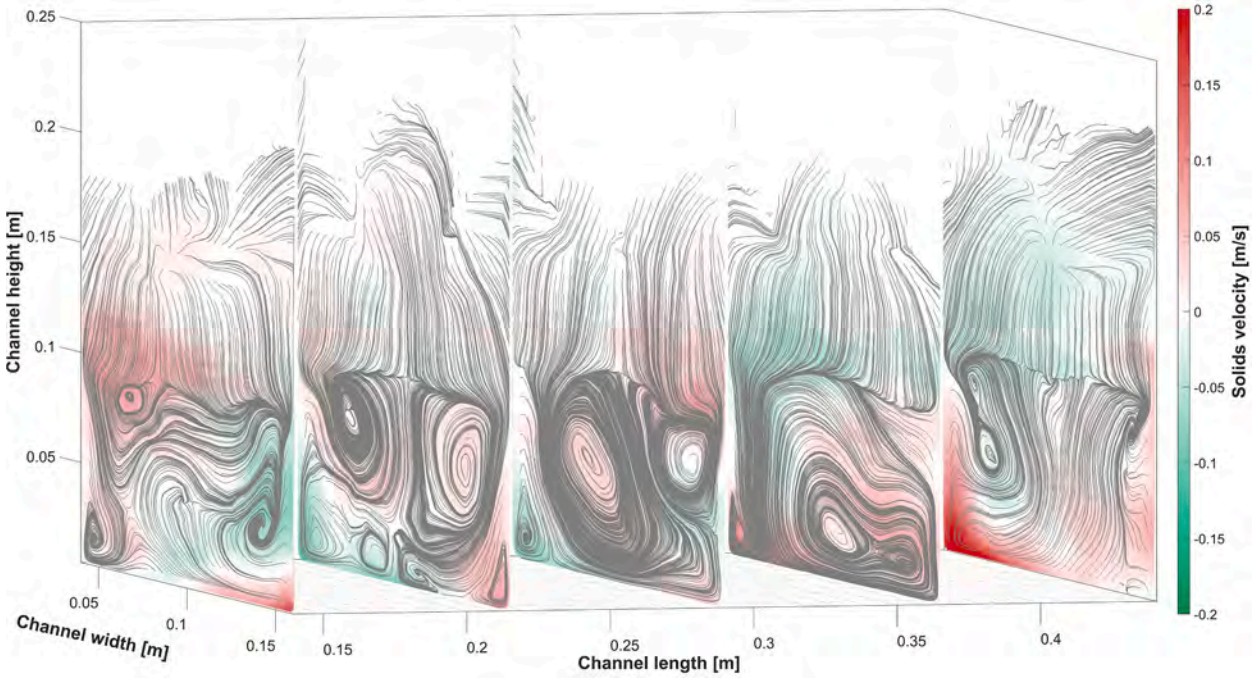

Fig. 10. Contour plots of the solids velocity profiles at different streamwise positions along the transport channel. Conditions: H=0.08 m; Q_{cz}=1.43 × 10^{-2} m^3/s.

dense bed surface and splash region, bubble eruptions eject particles upwards and outwards, imparting ballistic trajectories with significant lateral motion to the solids. A distinct zero-velocity crossing appears at an intermediate height, approximately halfway up the dense bed height. The corresponding profiles across the channel width (Fig. 8b) reveal asymmetric flow development and pronounced velocity gradients near the walls, suggesting strong wall effects and possible shear layer formation.

The corresponding profiles for the remaining operating conditions are provided in Appendix A.

Further insights into the data presented in Fig. 8 are provided by the solids flow pathlines for the same condition, as shown in Fig. 9, where the red and green segments indicate forward and reverse movements, respectively. These pathlines reveal the formation of coherent flow patterns, which are characterized by a sequence of vortices with alternating spin directions: the initial vortex is less distinct and spins clockwise, while the second vortex is clearly identified and spins counterclockwise. Analysis of all four cases (see Section 4.3.2) demonstrates that the operating conditions strongly influence the location, distinctness, and size of these vortex structures. At a low solids crossflow rate, stable vortices governing solids backmixing in the direction of flow are established. However, increasing the flowrate of the conveying air largely suppresses these recirculating zones.

Fig. 10 presents 2D representations of the streamwise solids velocity, $u_{s,x}$, at several positions along the channel for the same reference condition. Flow direction is indicated by colour (red for forward and, green for reverse velocities). Superimposed gray lines denote the streamlines of the local velocity field in the cross-sectional ($y-z$) plane, illustrating the organization and orientation of the vortex structures that promote circulation between the channel centerline and sidewalls. These structures develop in proximity to both walls and rotate in opposite directions, forming counter-rotating pairs that dominate the transverse

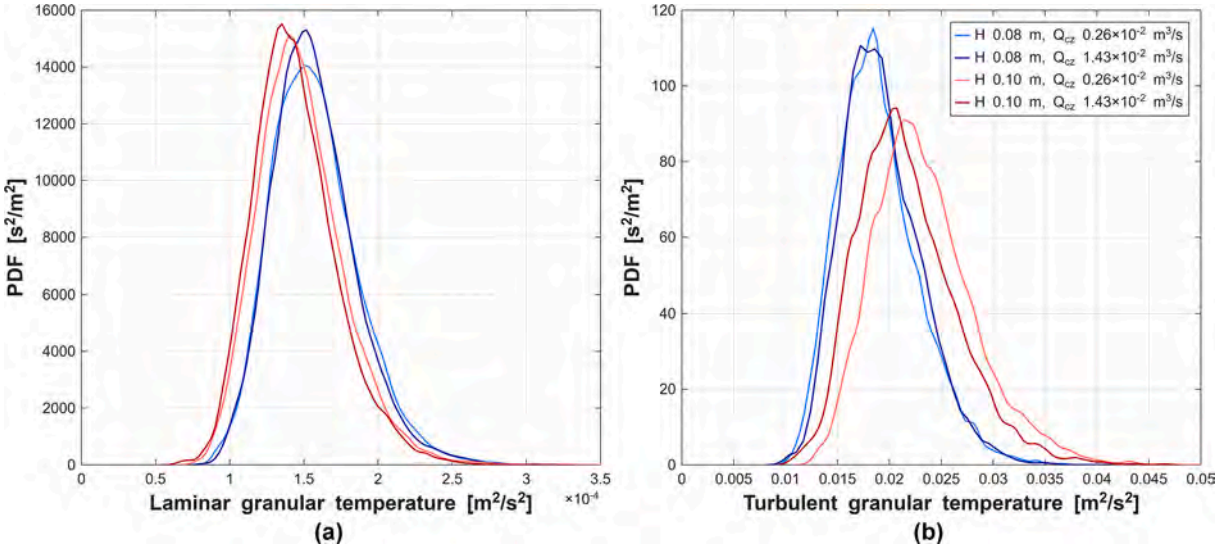

Fig. 11. Probability density functions of (a) laminar and (b) turbulent granular temperatures, for the four simulated conditions.

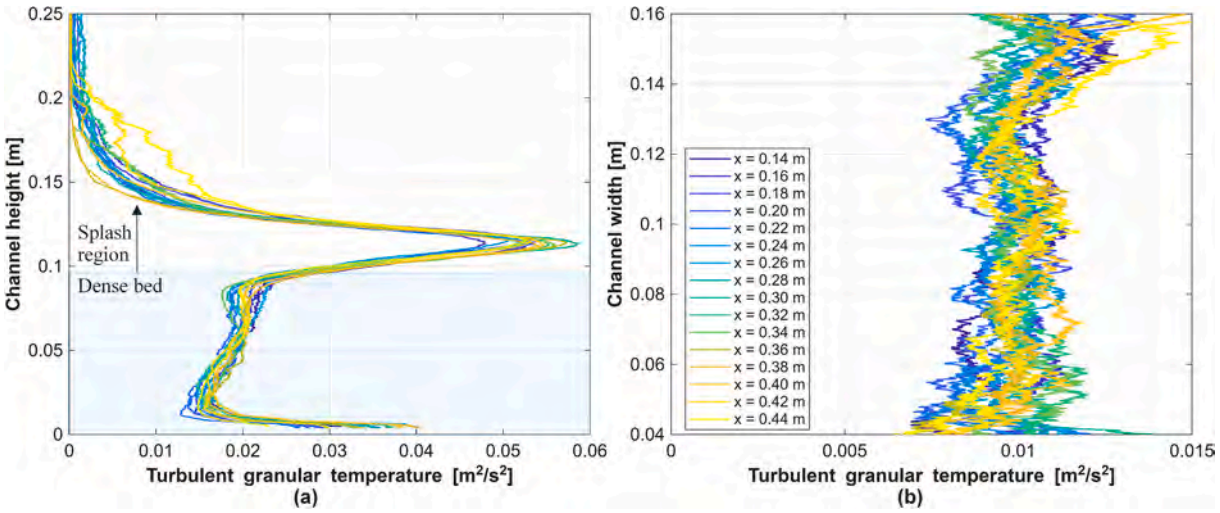

Fig. 12. Variation of turbulent granular temperature profiles at different streamwise positions with: (a) channel height; (b) channel width. Conditions: H=0.08 m; Q_{cz}=1.43 × 10^{-2} m^3/s.

flow in the *y-z* plane. Their interactions with the walls enhance local shear and promotes solids exchange between the near-wall and central regions, which in turn enhances lateral solids mixing. Analysis of the other conditions studied (Fig. A4) shows that a low solids crossflow is characterized by weak and disorganized vortices in the cross-sectional plane, whereas a higher solids crossflow promotes the formation of larger, more-coherent vortex patterns that span broader regions of the channel. This behavior contrasts with the previously noted suppressive effect of the solids crossflow rate on vortices aligned with the flow direction. Thus, increasing the solids crossflow primarily alters the orientations of vortex structures within the system.

4.3.2. Solids dispersion

4.3.2.1. Micro-scale dispersion. While granular temperature is closely linked to micro-scale dispersion, converting it to a dispersion coefficient requires knowledge of the spatial distribution of the collision frequency, which cannot be reliably determined from standard analytical expressions due to their limited validity scopes (e.g., for certain voidage ranges) [13,62]. Therefore, Fig. 11 the statistical distributions of the laminar and turbulent granular temperatures across the entire analysis region for the four simulated conditions. The laminar granular temperature is approximately two orders of magnitude lower than its turbulent counterpart, indicating that random particle motion and collisions have less-significant contributions to solids mixing than the turbulence induced by bubble motions and large-scale eddies. A comparable disparity between laminar and turbulent granular temperatures has been reported in stationary bubbling fluidized beds, where bubble-induced motion governs particle dispersion [68,84]. Thus, the data in Fig. 11 indicate that the presence of a solids crossflow preserves the same dominant mechanism for micro-scale mixing. Furthermore, the contribution of the turbulence mechanism increases with bed height.

Fig. 12 shows the profiles of the turbulent granular temperatures along the channel height (Fig. 12a) and width (Fig. 12b) at various streamwise positions. In Fig. 12a, micro-scale dispersive transport shows a local maximum immediately above the bottom plate, followed by a sharp decrease with height, and then a moderate increase along the dense bed, reaching a peak in the splash region due to bubble-induced solids ejection. Above the splash zone, dispersion decreases with height in the dilute region. This behavior persists along the entire channel length and aligns with previous experimental findings that highlight the strong influence of bubble eruption on horizontal solids mixing, which can account for 30–90% of the total mixing depending on the setup used [85–87]. Along the channel width (Fig. 12b), dispersion

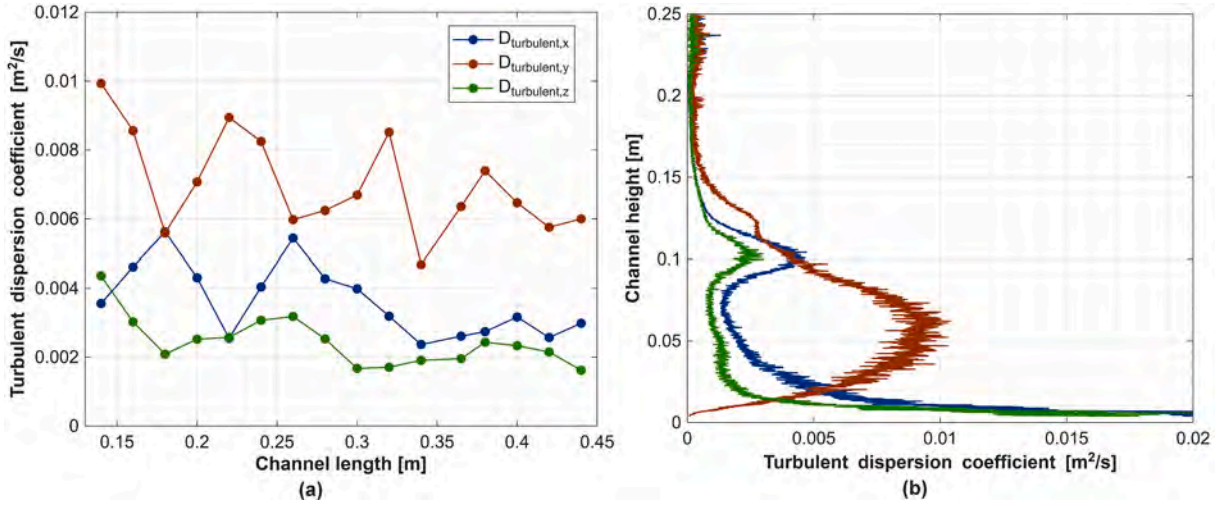

Fig. 13. Turbulent dispersion coefficient profiles in the streamwise (x), vertical (y) and lateral (z) directions, shown as functions of: (a) channel length; and (b) channel height. Conditions: H=0.08 m; Q_{cz}=1.43 × 10^{-2} m^3/s.

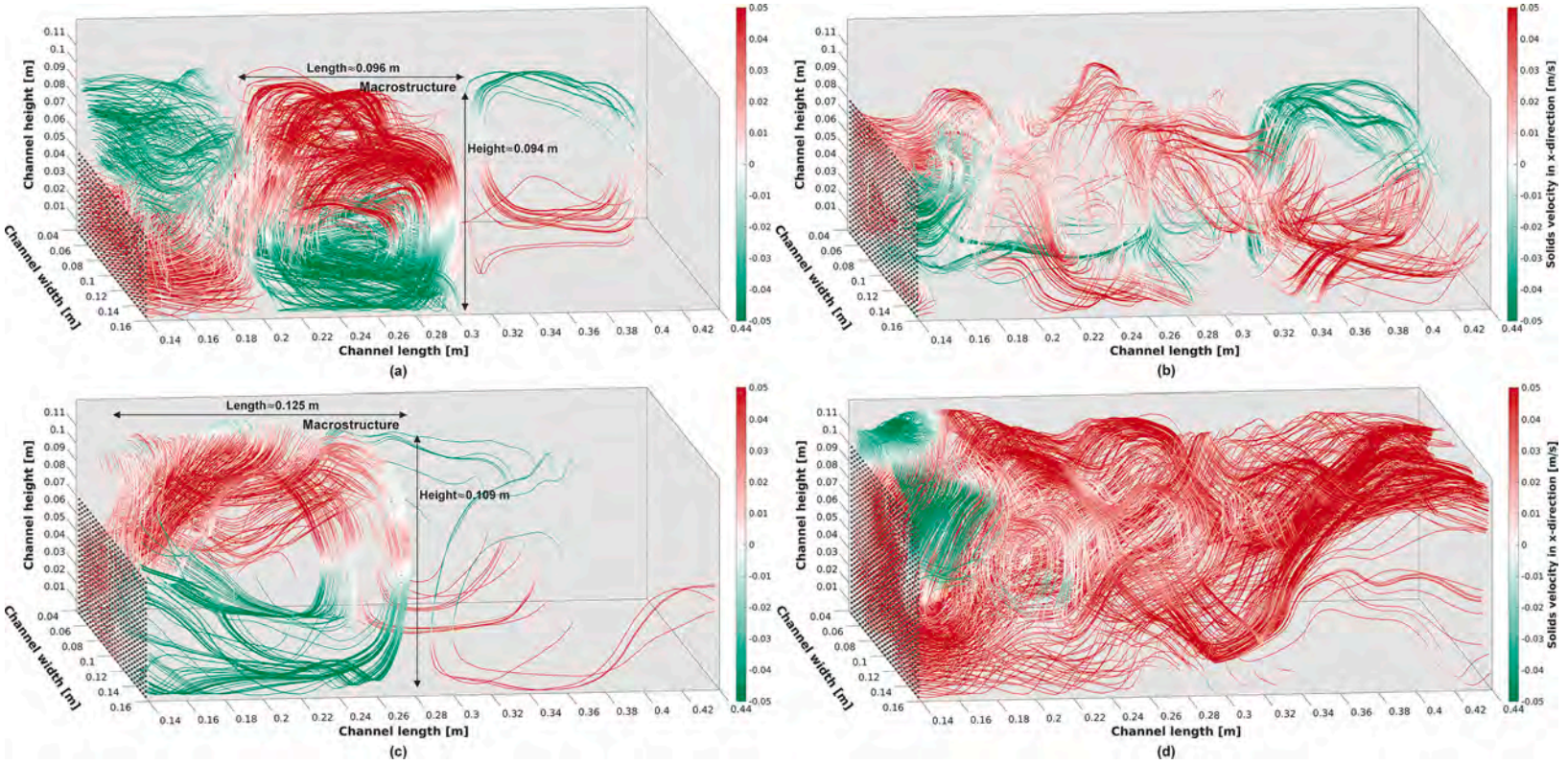

Fig. 14. Particle pathlines in the analysis region for the four tested conditions: (a) H=0.08 m, Q_{cz}=2.58 × 10^{-3} m^3/s; (b) H=0.08 m, Q_{cz}=1.43 × 10^{-2} m^3/s; (c) H=0.10 m, Q_{cz}=2.58 × 10^{-3} m^3/s; and (d) H=0.10, Q_{cz}=1.43 × 10^{-2} m^3/s.

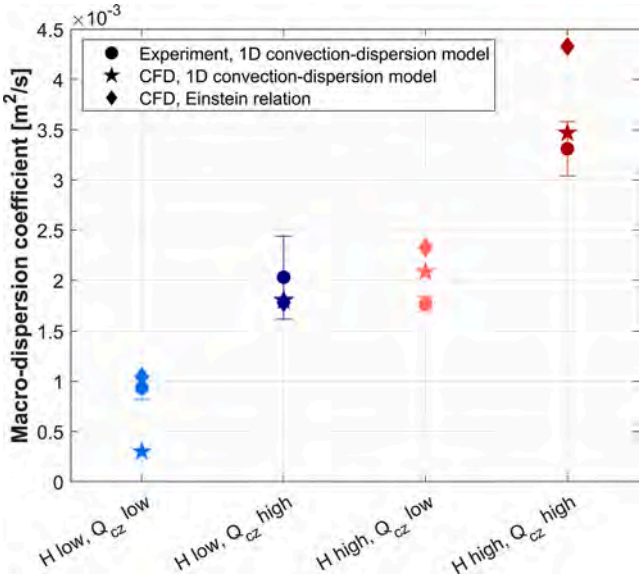

Fig. 15. Streamwise macro-dispersion coefficients for all tested conditions from CFD, compared with previously reported experimental data [28]. Note that dispersion coefficients in the vertical and lateral directions are not reported here, as motions in these directions are dominated by wall effects and large eddies comparable to the channel dimensions, which violates the assumptions underlying dispersive transport.

remains relatively uniform, with only minor deviations near the walls, suggesting the presence of laterally consistent bubble-induced mixing and limited wall effects within the channel core.

The turbulent dispersion coefficient can be analyzed separately for each direction based on Eq. (23). Fig. 13 shows the variations of its components along the channel length and height for a representative condition (i.e., low bed height and high flowrate of conveying air). The results for the other tested cases are provided in Appendix D; it is noteworthy that the impacts of operational parameters on micro-scale dispersion are very limited. Along the channel length, as shown in Fig. 13a, the three components of the turbulent dispersion coefficient remain relatively constant, with the vertical component consistently higher than the two horizontal components, which are comparable. This agrees with experimental studies that have reported faster dispersive mixing in the vertical direction than in the horizontal directions for bubbling fluidized beds [68,76]. The profiles along the channel height, shown in Fig. 13b, show similar trends for the two horizontal directions (streamwise and lateral): both components peak close to the bottom plate, decrease sharply in the lower bed, and remain relatively constant along the dense bed height, with a local maximum in the splash region just above the dense bed surface due to bubble eruptions. In contrast, the vertical dispersion component starts from zero at the distributor plate, increases with height to reach its highest level within the dense bed, and decreases close to the dense bed surface. In summary, horizontal solids dispersion occurs mainly near the bottom plate and at the dense bed surface, while vertical dispersion is most pronounced within the bulk of the dense bed. This is consistent with the qualitative description of gas-solid flow provided in Section 2.3: as bubbles form and rise, they entrain and displace solids vertically within their wakes, while bubble formation at the bottom plate and eruption at the dense bed surface are the primary contributors to horizontal dispersion.

4.3.2.2. Macro-scale dispersion. Fig. 14 illustrates the particle pathlines for the four tested conditions, enabling examinations of macro-scale solids dispersion within the analysis region. The pathlines are colour-coded by the x-component of the time-averaged velocity field, with red indicating forward motion, green indicating reverse motion, and white denoting regions of near-zero streamwise velocity. For the two low-crossflow conditions, well-defined macrostructures are evident, consistent with the large-scale vortex recirculation zones identified previously (see Fig. 9). The visualization further shows that the size of these macrostructures increases with bed height, which explains the observed increase in dispersion with bed height. Increasing the solids crossflow largely disrupts the distinct recirculation vortices seen at low crossflow rates and in stationary beds, resulting in more-elongated pathlines with low structural coherence, indicative of a longer characteristic mixing length and enhanced internal mixing.

These qualitative trends are corroborated by the quantitative metrics presented in Appendix E. For the low crossflow cases, the macrostructure region increases in both streamwise length and vertical extent with bed height: from 0.096 m to 0.125 m in length (~30% increase), and from 0.094 m to 0.109 m in height (~16% increase). The characteristic recirculation loop period similarly increases from 1.9 s to 3.6 s, reflecting the longer circulation times within larger vortices. For these cases, the average dispersion coefficient calculated from the Einstein relation is approximately 1.91×10^{-3} m^2/s. The tortuosity metric, which quantifies the degree to which particle trajectories deviate from a straight path, captures the progressive transition in flow structure across conditions (see Fig. A10). High mean tortuosity values are observed for the low crossflow cases (27.48 at H=0.08 m and 7.33 at H=0.10 m), consistent with the dominance of multiloop recirculating motion. As either bed height or crossflow increases, tortuosity values decrease (down to ~1.97), indicating increasingly direct particle trajectories as macrostructural coherence is lost.

Fig. 15 compares the streamwise macro-dispersion coefficients, $D_{macro,x}$, obtained from the CFD data using two methods: (1) fitting to a transient 1D convection-dispersion model (Table 4), and (2) applying the Einstein relation (Eq. (21)) to the particle pathline data (Fig. 14). These results are shown alongside using experimentally derived values from a previous study [28] for all the tested conditions. The two methods yield similar results for each condition. The macro-scale dispersion coefficient increases with both bed height and solids crossflow rate. The increase in dispersion with bed height is consistent with previous findings, whereby larger bubbles promote more-vigorous particle ejection upon eruption [88]. This also aligns with the results depicted in Fig. 14 of the present work, which show that a taller dense bed produces larger vortex flow structures, corresponding to the establishment of larger bubbles. Increased dispersion at higher solids convection rates is similarly explained by the evolution of flow macrostructures. At low crossflow rates, particle motion primarily follows compact, coherent flow patterns, such that the characteristic transport length is limited by the size and residence time of these structures. Consequently, under these conditions, the limited transport length and strong localization of flow patterns contribute to the persistence of dead zones, as particles remain confined to restricted regions within the bed. As the crossflow rate increases, the simulated CFD data show that these structures become more disrupted, elongated, and less coherent. This causes the particles to follow longer, less-streamlined paths, resulting in higher dispersion rates. As a result, the extent of dead zones decreases, since particles can access and circulate through regions of the bed that would otherwise remain stagnant at lower crossflow rates. This observation is consistent with previous work [28], where an increase in crossflow was shown to reduce the extent of dead zones, as quantified in that study.

5. Conclusions

This study employs Eulerian-Eulerian CFD modeling, validated against experimental data, to perform a spatially-resolved analysis of the mechanisms underlying solids transport in a bubbling fluidized bed with horizontal crossflow of solids. Comprehensive mapping of spatially-resolved velocity and dispersion fields, including flow structures, was used to characterize the flow behaviors and the relationships between these parameters at the macro-scale.

At low crossflow rates, solids flow is organized into counter-rotating vortical structures. This results in a velocity field in which the crossflow component reaches a maximum near both the bottom plate and the dense bed surface, although in opposite directions. Consequently, solids backmixing along the crossflow direction occurs alternately at these locations as the solids flow develops downstream. While lower crossflow rates were associated with frequent solids recirculation within these vortex structures, increasing the crossflow progressively disrupts the coherent vortices, resulting in more-pronounced forward transport and elongated particle paths with reduced levels of coherence (and, thus, greater mixing). This disruption leads to higher macroscopic dispersion coefficients at high crossflow rates, in accord with both the present simulations and previous experimental findings. In addition, increased bed height further enlarges the macrostructures. The lateral solids velocity profiles exhibited pronounced asymmetry and steep gradients near the channel walls.

The micro-scale dispersion analysis showed that turbulent dispersion is approximately two orders of magnitude greater than its laminar counterpart, indicating that solids mixing at this scale is governed primarily by the bubble dynamics and particle clusters, rather than by random particle motions or collisions. The vertical component of turbulent dispersion peaked at mid-height in the dense bed and was slightly higher than the horizontal components. Horizontal dispersion exhibited maxima near the gas distributor and dense bed surface, highlighting bubble wake formation at the site of gas injection and bubble eruption at the bed surface as the main mechanisms for solids horizontal mixing. The lateral profiles of turbulent dispersion remained largely uniform, indicating a negligible wall influence.

Nomenclature

C_D	Drag coefficient[−]
D	Solids dispersion coefficient[m^2/s]
D_b	Equivalent bed diameter[m]
d_p	Mean particle diameter[m]
e	Coefficient of restitution[−]
Fr	Froude number[−]
G_s	Solids' circulation rate[kg/(m^{2}s)]
g	Gravity constant, 9.81[m/s^2]
g_0	Radial distribution function[−]
H	Bed height[m]
I_{2D}	2nd invariant of the deviator of the rate of strain tensor[s^{-2}]
L	Length[m]
P	Pressure[Pa]
PSD	Particle size distribution[−]
Q_{cz}	Volumetric flowrate of air in the conveying zone[m^3/s]
Δr^{disp}	Particle displacement attributable to dispersion[m]
Re	Reynolds number[−]
t	Time[s]
u	Velocity[m/s]
u'	Velocity fluctuation[m/s]
u_0	Fluidization velocity[m/s]
u_{mf}	Minimum fluidization velocity[m/s]
x, y, z	Cartesian coordinate system axes: x/z lie in the horizontal plane, y is vertical[m]

Greek letters

β_{gs}	Inter-phase momentum exchange coefficient[kg/(m^{3}s)]
γ_{θ_s}	Granular collision energy dissipation[kg/(ms^3)]
ε	Volume fraction[−]
θ_s	Granular temperature[m^2/s^2]
κ_{θ_s}	Granular energy conductivity[kg/(ms)]
μ	Viscosity[kg/(ms)]
$\mu_{s,c}$	Collisional part of the solids shear viscosity[kg/(ms)]
$\mu_{s,f}$	Frictional part of the solids shear viscosity[kg/(ms)]
$\mu_{s,k}$	Kinetic part of the solids shear viscosity[kg/(ms)]
ξ	Bulk viscosity[kg/(ms)]
ρ	Density[kg/m^3]
$\bar{\tau}$	Stress tensor[Pa]
τ_L	Lagrangian integral time scale[s]
φ	Particle sphericity[−]
φ_f	Angle of internal friction[−]

Subscripts

cz	Conveying zone
g	Gas phase
s	Solid phase
macro	Macro-scale

CRediT authorship contribution statement

Munavara Farha: Writing – original draft, Validation, Methodology, Investigation, Formal analysis, Conceptualization. **Henrik Ström:** Writing – review & editing, Supervision. **Diana Carolina Guío-Pérez:** Writing – review & editing, Supervision. **David Pallarès:** Writing – review & editing, Supervision, Funding acquisition.

Declaration of competing interest

The authors declare the following financial interests/personal relationships which may be considered as potential competing interests:

David Pallares reports financial support was provided by Swedish Energy Agency. If there are other authors, they declare that they have no known competing financial interests or personal relationships that could have appeared to influence the work reported in this paper.

Acknowledgments

The authors acknowledge the financial support provided by the Swedish Energy Agency within the framework of project no. 51182-1 - *Thermochemical poly-generation in heat and power plants*. The contribution of RISE Sensor Systems is also acknowledged, as it made possible the development of the Magnetic Solids Tracing system used in this work. The computations using the ANSYS Fluent software were enabled by resources provided by the National Academic Infrastructure for Supercomputing in Sweden (NAISS), partially funded by the Swedish Research Council (grant no. 2022-06725).

Appendix A

Figs. A1 and A2 show the crossflow component of solids velocity at various streamwise positions under four tested operating conditions. In Fig. A1, the profiles are plotted as a function of bed height (mass-weighted over the channel width), whereas Fig. A2 presents the data as a function of channel width (mass-weighted over the bed height).

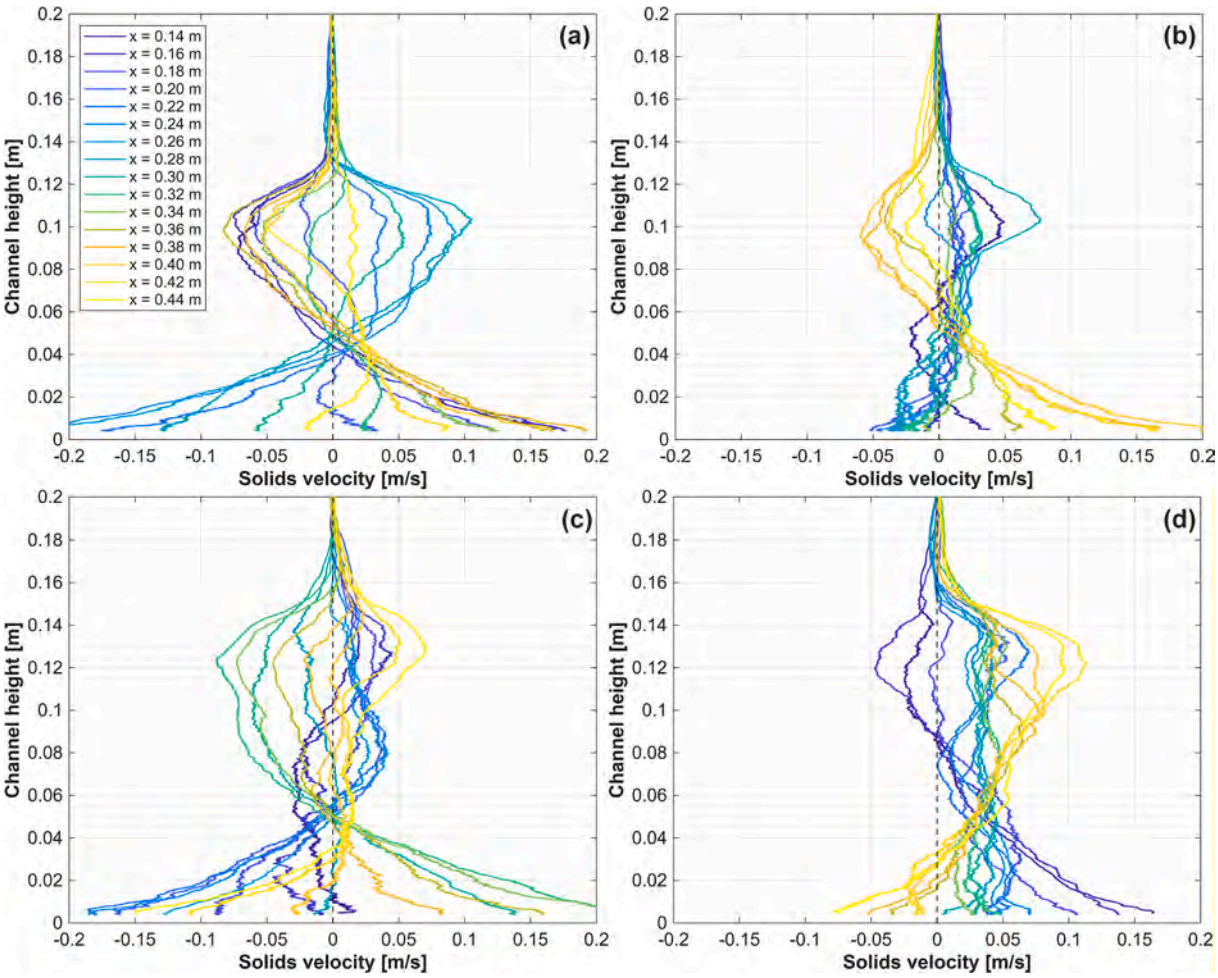

Fig. A1. Profiles of the solids velocity in the flow direction at different streamwise positions, showing variation with channel height for the four tested conditions: (a) H=0.08 m, Q_{cz}=2.58 × 10^{-3} m^3/s; (b) H=0.08 m, Q_{cz}=1.43 × 10^{-2} m^3/s; (c) H=0.10 m, Q_{cz}=2.58 × 10^{-3} m^3/s; and (d) H=0.10 m, Q_{cz}=1.43 × 10^{-2} m^3/s.

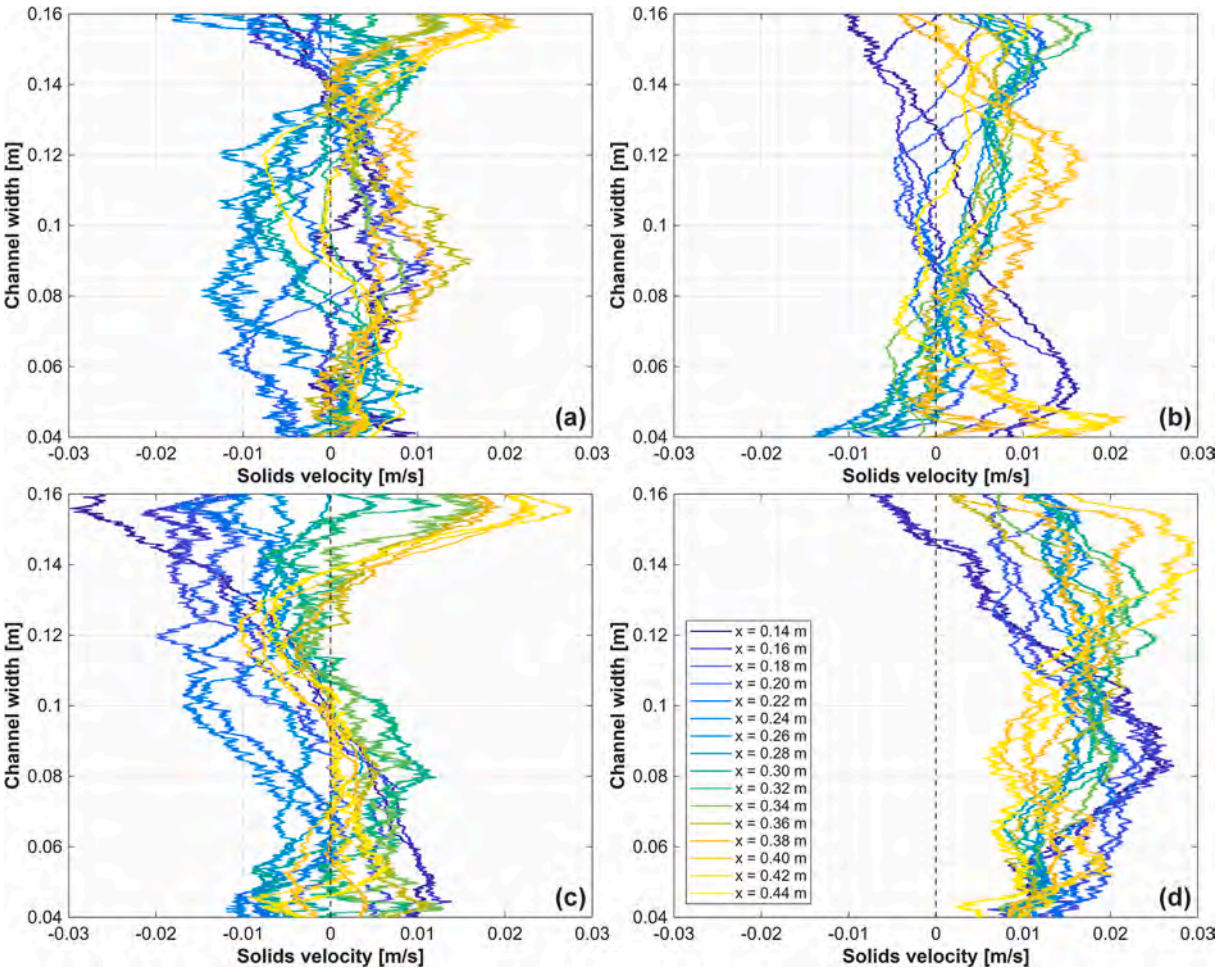

Fig. A2. Profiles of the solids velocity in the flow direction at different streamwise positions, showing variation with channel width for the four tested conditions: (a) H=0.08 m, Q_{cz}=2.58 × 10^{-3} m^3/s; (b) H=0.08 m, Q_{cz}=1.43 × 10^{-2} m^3/s; (c) H=0.10 m, Q_{cz}=2.58 × 10^{-3} m^3/s; and (d) H=0.10 m, Q_{cz}=1.43 × 10^{-2} m^3/s.

Appendix B

To further characterize solids transport, the extent of solids backmixing was quantified. Fig. A3 shows the relative ratio of forward to backward solids flow at various streamwise positions for the four tested conditions. The net forward solids transport prevails at high conveying velocity, especially with increased bed height. Conversely, the combination of high bed height and low conveying velocity results in the most pronounced backward flow.

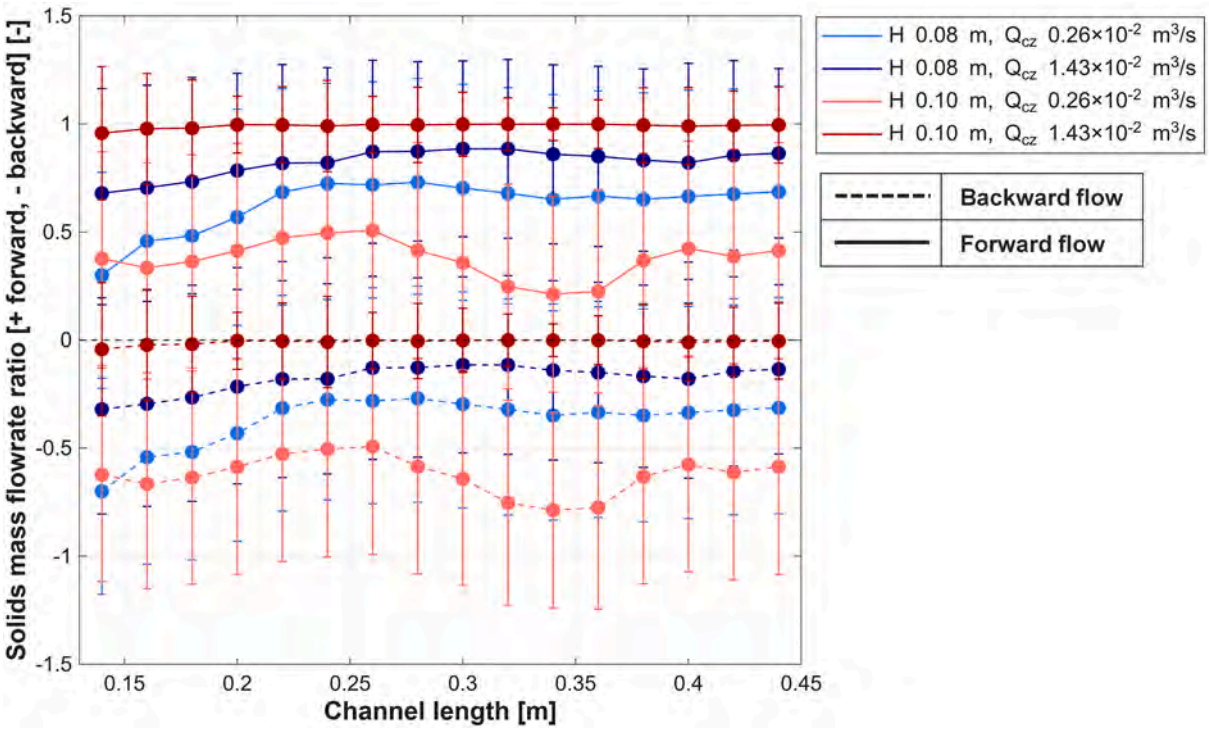

Fig. A3. Quantification of solids backmixing at different streamwise positions for four experimental conditions. Solid lines indicate the ratio of forward solids flow, while dotted lines represent backward flow.

Appendix C

Figs. A4 and A5 present the spatial distributions of the solids velocity and turbulent granular temperature, respectively, for the four tested conditions. The 2D turbulent granular temperature fields exhibit pronounced spatial heterogeneity, with higher values concentrated around the splash region, where dispersion is particularly evident due to intense particle motion and bubble activity

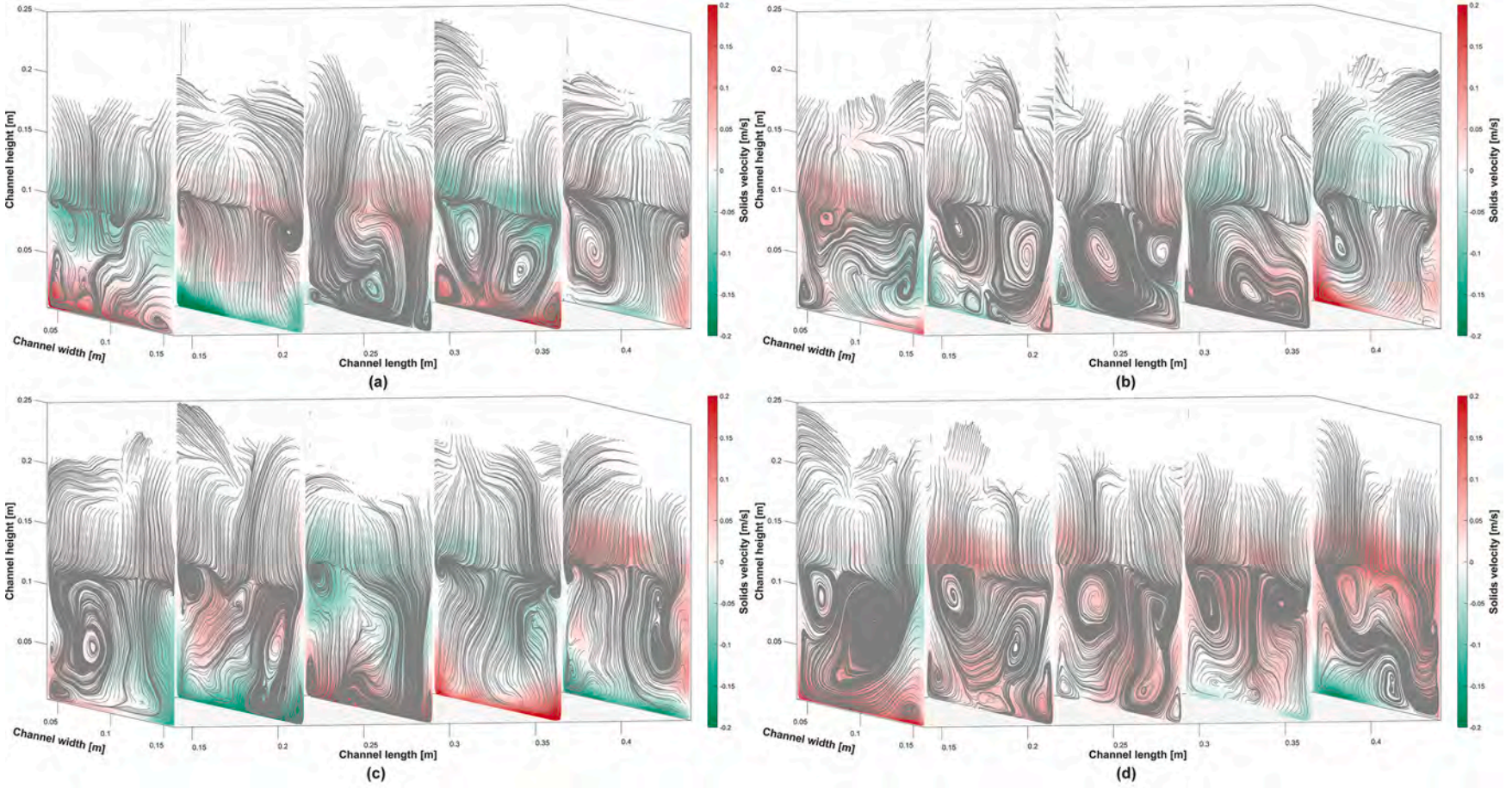

Fig. A4. Solids velocity profiles across channel cross-sections at five positions along the transport channel for the four tested conditions: (a) H=0.08 m, Q_{cz}=2.58 × 10^{-3} m^3/s; (b) H=0.08 m, Q_{cz}=1.43 × 10^{-2} m^3/s; (c) H=0.10 m, Q_{cz}=2.58 × 10^{-3} m^3/s; and (d) H=0.10 m, Q_{cz}=1.43 × 10^{-2} m^3/s.

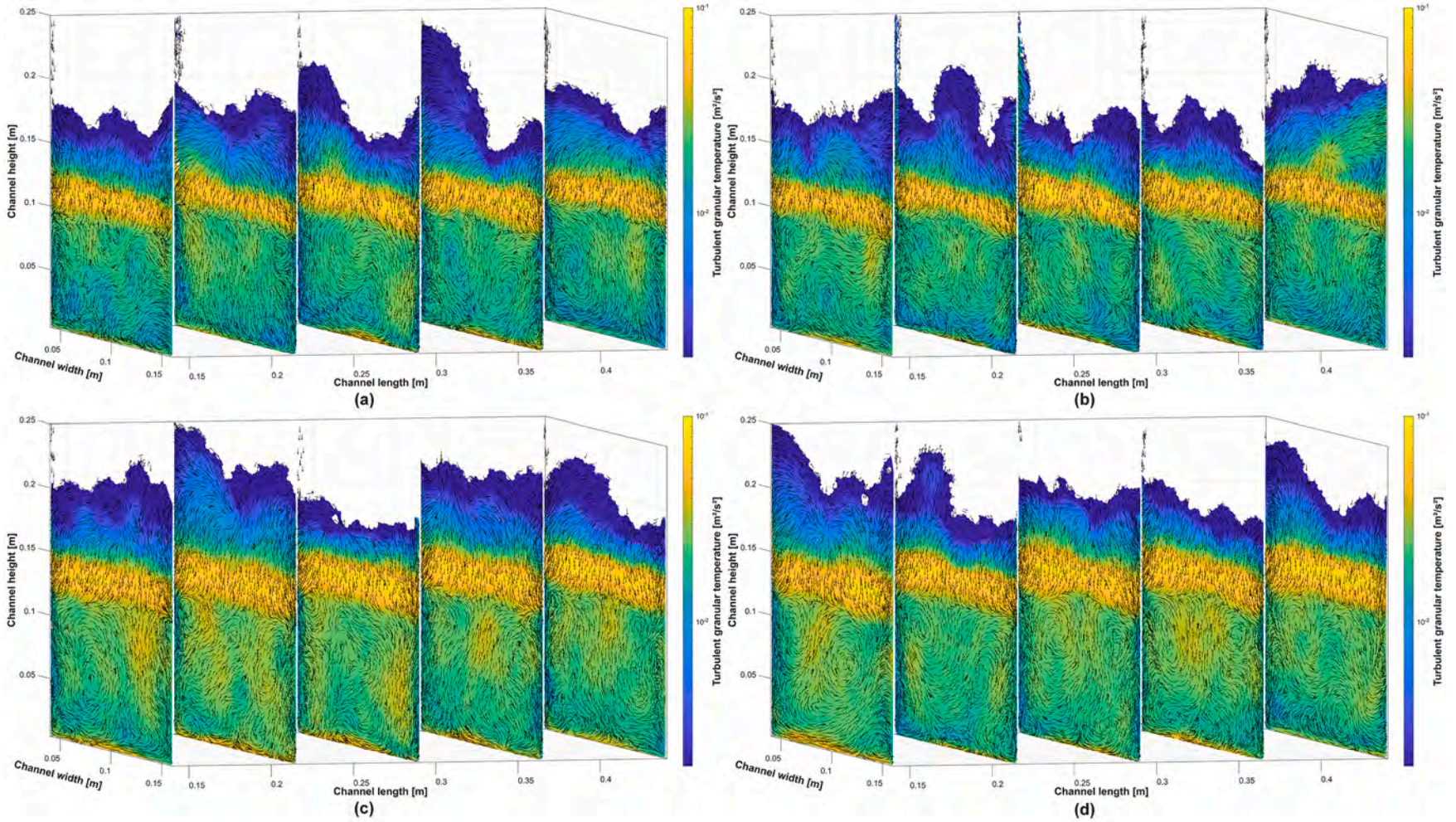

Fig. A5. Turbulent granular temperature maps across channel cross-sections at five positions along the transport channel for the four tested conditions: (a) H=0.08 m, Q_{cz}=2.58 × 10^{-3} m^3/s; (b) H=0.08 m, Q_{cz}=1.43 × 10^{-2} m^3/s; (c) H=0.10 m, Q_{cz}=2.58 × 10^{-3} m^3/s; and (d) H=0.10 m, Q_{cz}=1.43 × 10^{-2} m^3/s.

Appendix D

Fig. A6 presents the turbulent dispersion coefficients and the corresponding characteristic cluster lengths in the streamwise, vertical, and lateral directions for the four tested conditions. Both quantities are plotted along the channel length, with the turbulent dispersion coefficient shown on the primary *y*-axis and the characteristic cluster length represented on the secondary *y*-axis

The characteristic length of the particle clusters quantifies the spatial scale of the correlated particle motion in each direction and is given by the following equation [51,62,72]:

$$L_{turbulent,i} = \frac{D_{turbulent,i}}{\sqrt{\overline{u'_{s,i}u'_{s,i}}}} \tag{A1}$$

The characteristic cluster length is generally highest in the vertical direction, followed by the streamwise direction, and lowest in the lateral direction.

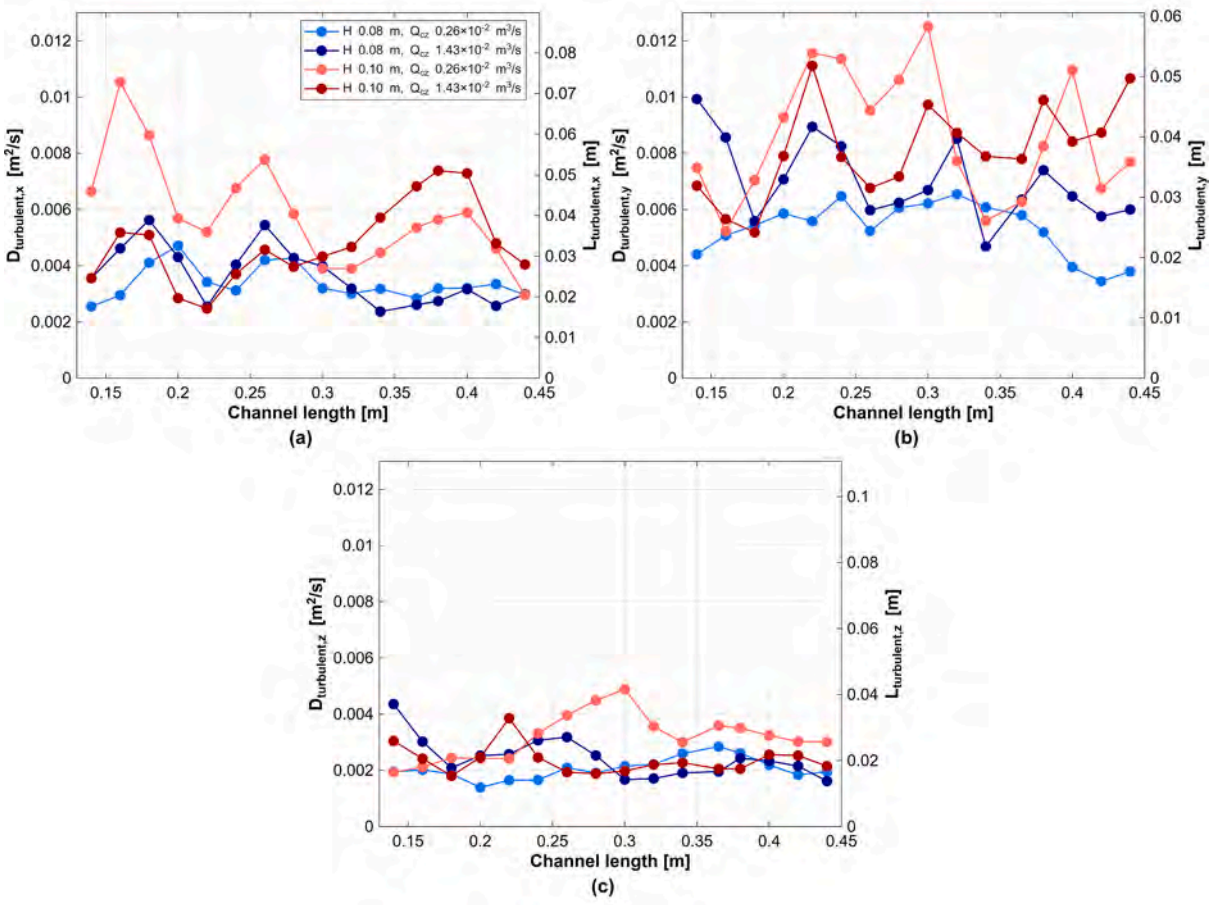

Fig. A6. Turbulent dispersion coefficient (primary *y*-axis) and characteristic cluster length (secondary *y*-axis) along the channel length for the four tested conditions: (a) streamwise direction; (b) vertical direction; and (c) lateral direction.

Fig. A7 presents the profiles of the turbulent dispersion coefficients along the channel height for the streamwise ($D_{turbulent,x}$), vertical ($D_{turbulent,y}$), and lateral ($D_{turbulent,z}$) components for all four tested conditions.

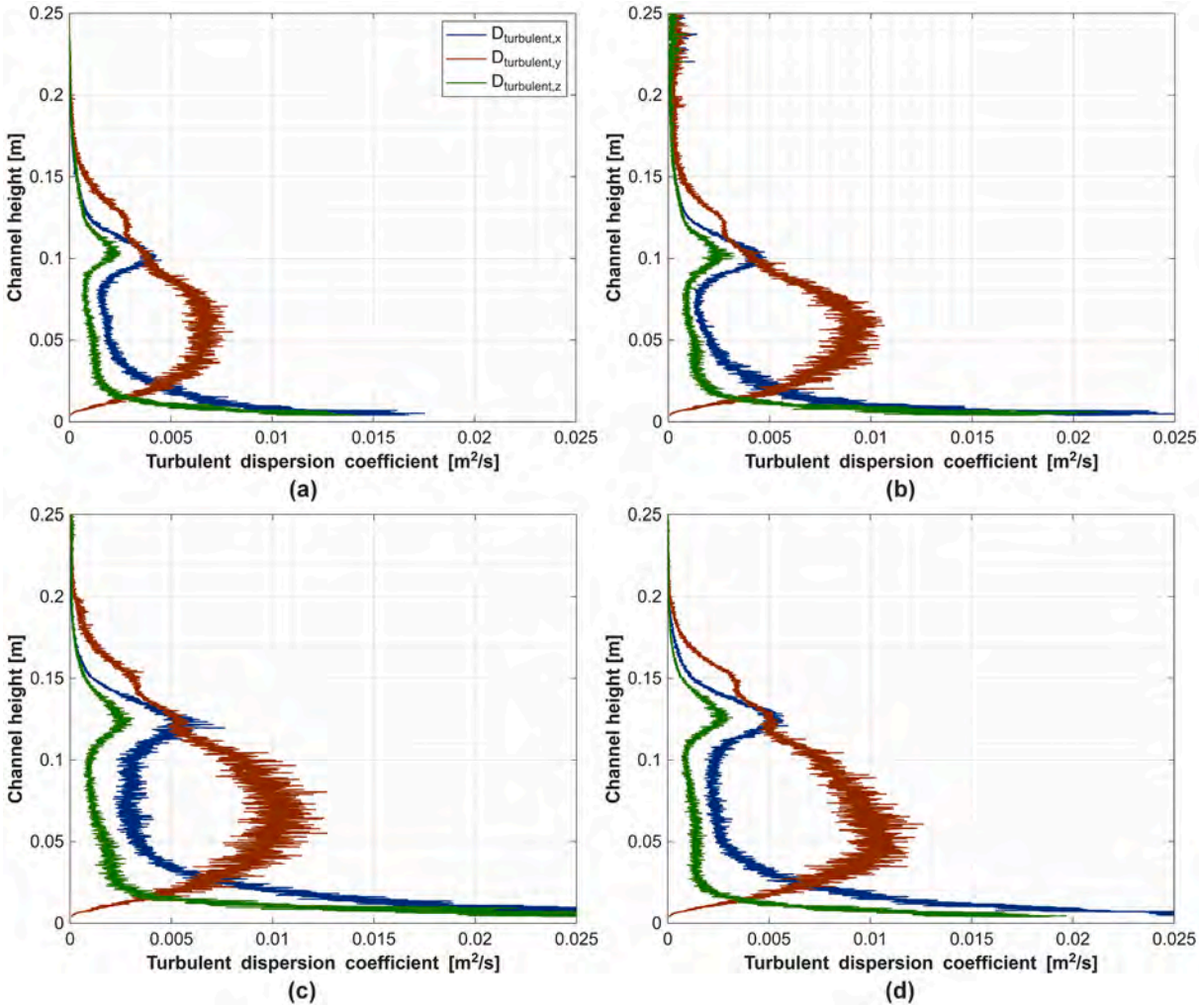

Fig. A7. Profiles of the turbulent dispersion coefficients in the streamwise, vertical, and lateral directions as a function of channel height for the four tested conditions: (a) H=0.08 m, Q_{cz}=2.58 × 10^{-3} m^3/s; (b) H=0.08 m, Q_{cz}=1.43 × 10^{-2} m^3/s; (c) H=0.10 m, Q_{cz}=2.58 × 10^{-3} m^3/s; and (d) H=0.10 m, Q_{cz}=1.43 × 10^{-2} m^3/s.

Table A1 summarizes the turbulent dispersion coefficients for the four tested conditions. While the operational parameters show some influences, their overall impact on micro-scale dispersion is limited, with only moderate variations being observed.

Table A1
Turbulent dispersion coefficients in streamwise, vertical, and lateral directions.

Condition		Turbulent dispersion coefficient [m^2/s]		
H [m]	Q_{CZ} [m^3/s]	$D_{turbulent.x}$	$D_{turbulent.y}$	$D_{turbulent.z}$
0.08	2.58 × 10^{-3}	(3.39 ± 0.60) × 10^{-3}	(5.32 ± 0.97) × 10^{-3}	(2.06 ± 0.38) × 10^{-3}
0.08	1.43 × 10^{-2}	(3.63 ± 1.03) × 10^{-3}	(7.03 ± 1.44) × 10^{-3}	(2.45 ± 0.71) × 10^{-3}
0.10	2.58 × 10^{-3}	(5.86 ± 1.91) × 10^{-3}	(8.62 ± 2.27) × 10^{-3}	(3.18 ± 0.82) × 10^{-3}
0.10	1.43 × 10^{-2}	(4.78 ± 1.45) × 10^{-3}	(8.15 ± 1.66) × 10^{-3}	(2.35 ± 0.51) × 10^{-3}

Appendix E

The structural features of solids flow within the analysis domain are quantitatively characterized using three principal metrics: macrostructure size, recirculation loop period, and tortuosity. The methodology and defining equations for each metric are outlined below. Metrics requiring the identification of a coherent macrostructure (i.e., macrostructure size and recirculation loop period) are reported only for low crossflow conditions, where such structures are present.

The macrostructure region is identified by analyzing the distribution of streamwise (x) positions where particle pathlines exhibit directional reversals. A histogram of these reversal positions is constructed, and the macrostructure is defined as the contiguous region in $\boldsymbol{x}$ where the frequency of reversals exceeds a chosen percentile threshold (typically the 90th percentile).

For each traversing pathline within this region, the x- and y-spans are computed, and the average macrostructure length and height are given by:

$$L_{macro} = \frac{1}{N}\sum_{k=1}^{N}\left[max(x_k) - min(x_k)\right] \tag{A2}$$

$$H_{macro} = \frac{1}{N}\sum_{k=1}^{N}\left[max(y_k) - min(y_k)\right] \tag{A3}$$

Here, $max(x_k)$ and $\min(x_k)$ (and likewise for y_k) are evaluated over all points of segment k that lie within the identified macrostructure region, and N is the number of such traversing segments.

The recirculation loop period quantifies the characteristic time for a particle to complete one full recirculation loop within the macrostructure. For each traversing pathline, local minima and maxima in the x-coordinate were identified as reversal points, i.e., locations where the direction of motion in x changes. Candidate loops were defined as trajectory segments between consecutive reversal points, and only those with a net displacement in x exceeding 99% of the identified macrostructure width were included. The loop period was calculated as the number of time steps between these two reversal points, multiplied by the integration time step.

The resulting distributions of recirculation loop periods for low crossflow conditions at two different bed heights are shown in Fig. A8. At low bed height, the mean recirculation loop period is approximately 1.9 s, while at high bed height it increases to 3.6 s.

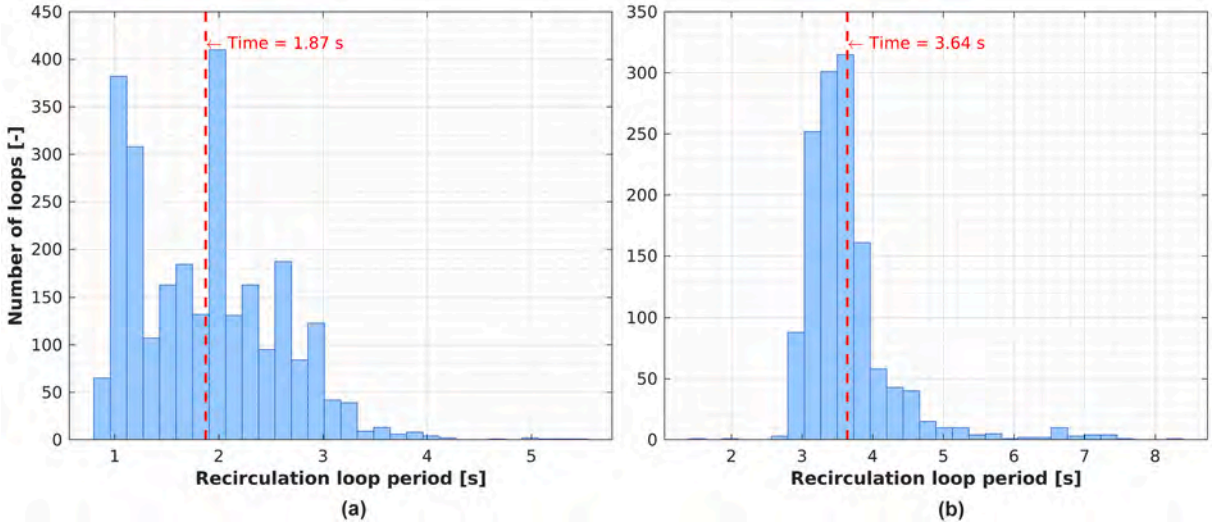

Fig. A8. Distributions of recirculation loop periods extracted from particle pathlines for the low crossflow conditions at two different bed heights: (a) 0.08 m and (b) 0.10 m. The dashed red lines indicate the mean recirculation loop period for each case. (For interpretation of the references to colour in this figure legend, the reader is referred to the web version of this article.)

Tortuosity is defined as the ratio of the total arc length of a particle pathline to the straight-line (Euclidean) distance between its starting and ending positions, providing a direct measure of the path's winding or convolutedness. A tortuosity value of unity indicates a perfectly straight trajectory, while values greater than one reflects increasingly winding or convoluted paths. This metric can be evaluated for all pathlines, irrespective of the presence or absence of a macrostructure.

For each particle pathline, the tortuosity is given by:

$$T = \frac{1}{N}\sum_{k=1}^{N}\frac{L_k^{arc}}{L_k^{euclid}} \tag{A4}$$

where,

L_k^{arc} is the total arc length of the k-th particle pathline, calculated as the sum of the distances between each pair of consecutive points along the trajectory:

$$L_k^{arc} = \sum_{p=1}^{P_k-1}\sqrt{\left(x_{p+1}-x_p\right)^2 + \left(y_{p+1}-y_p\right)^2 + \left(z_{p+1}-z_p\right)^2} \tag{A5}$$

Here, p indexes the time steps and P_k is the total number of recorded points for the pathline.

L_k^{euclid} is the straight-line (Euclidean) distance between the initial and final positions of the pathline:

$$L_k^{euclid} = \sqrt{\left(x_{k,end}-x_{k,start}\right)^2 + \left(y_{k,end}-y_{k,start}\right)^2 + \left(z_{k,end}-z_{k,start}\right)^2} \tag{A6}$$

Notably, for each pathline, L_k^{euclid} is a single value that quantifies the net displacement from entry to exit.

Fig. A9 visually demonstrates the calculation of tortuosity for a representative particle pathline. The blue curve traces the actual 3D trajectory of a single particle through the channel, illustrating the complex, winding nature of its motion. The total arc length, L_k^{arc}, is indicated by the full length of the blue path, capturing all the intermediate bends and turns. The straight-line (Euclidean) distance, L_k^{euclid}, is shown as the red dotted line directly connecting the entry ("Start") and exit ("End") points of the pathline.

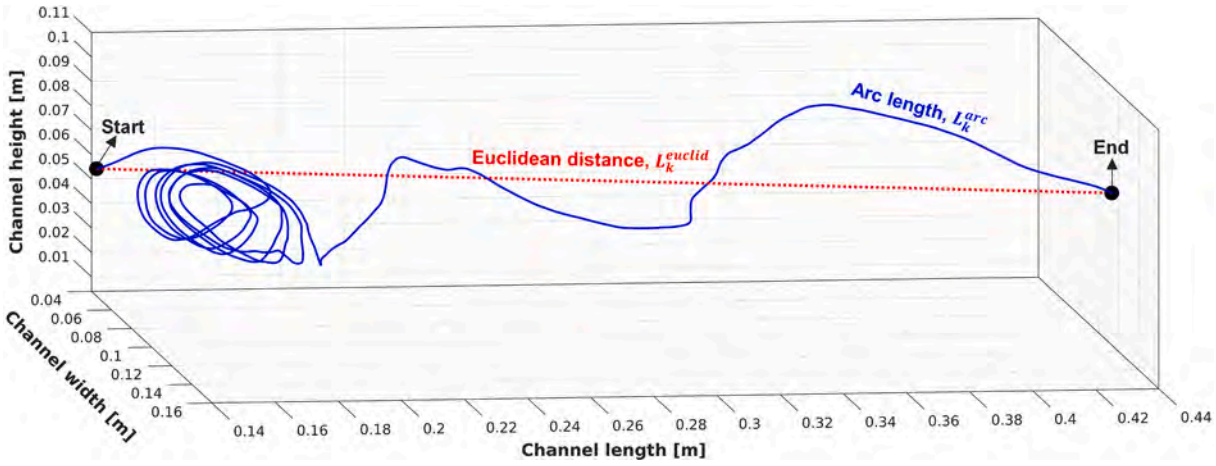

Fig. A9. Visualization of tortuosity calculation for a representative particle pathline. For this example, L_k^{arc}=1.42, L_k^{euclid}=0.31, and T=4.60.

Fig. A10 presents the distributions of particle pathline tortuosity for all four tested conditions. For the low crossflow cases (a, c), the distributions are centered at high values, reflecting the dominance of macro-scale recirculation structures that force particles along highly winding paths. The reduction in mean tortuosity with increasing bed height suggests that more particles can traverse the channel with fewer recirculation events as the macrostructure enlarges. In contrast, for the high crossflow cases (b, d), the distributions are shifted toward lower tortuosity, indicating that most particles follow more direct, streamwise-oriented trajectories as the crossflow disrupts coherent vortex structures. The lowest tortuosity values are observed at the highest bed height and crossflow, where macrostructural coherence is nearly absent.

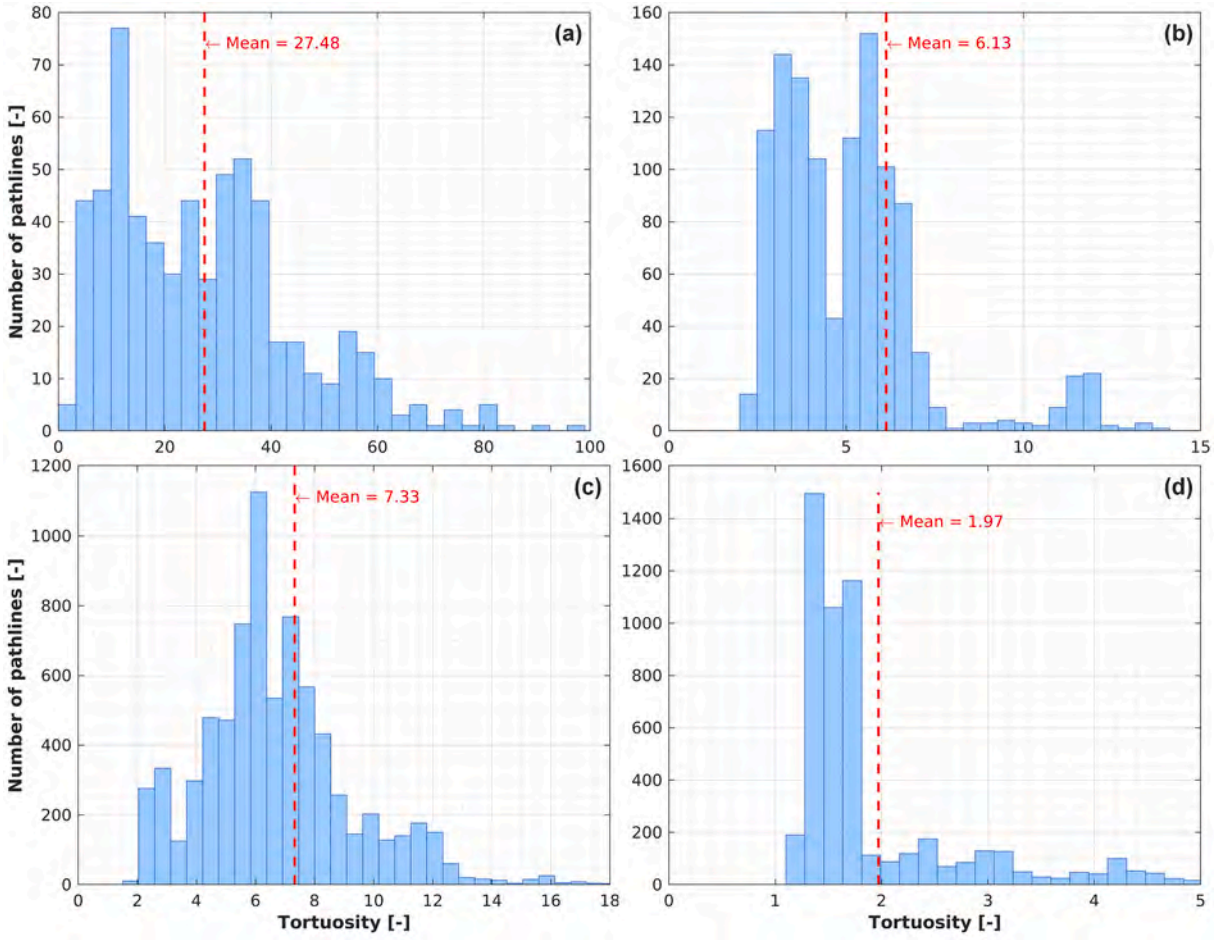

Fig. A10. Distributions of particle pathline tortuosity for all four tested conditions: (a) H=0.08 m, Q_{cz}=2.58 × 10^{-3} m^3/s; (b) H=0.08 m, Q_{cz}=1.43 × 10^{-2} m^3/s; (c) H=0.10 m, Q_{cz}=2.58 × 10^{-3} m^3/s; and (d) H=0.10, Q_{cz}=1.43 × 10^{-2} m^3/s. Mean tortuosity values are indicated by dashed lines.

Appendix F

Fig. A11 presents the time evolution of the mean squared displacement (MSD) in the streamwise (x) direction for all individual tracked particle pathlines in the four tested cases. In all cases, the value of Δx^2 increases with time and eventually approaches a constant value, consistent with the development and eventual saturation of particle dispersion in the bed [10,65–67]. The slope of the linear region is used to estimate the macro-scale dispersion coefficient, as discussed in Section 0. The trajectories are subsequently volume-fraction weighted and ensemble-averaged according to the Einstein relation (see Eq. (21))

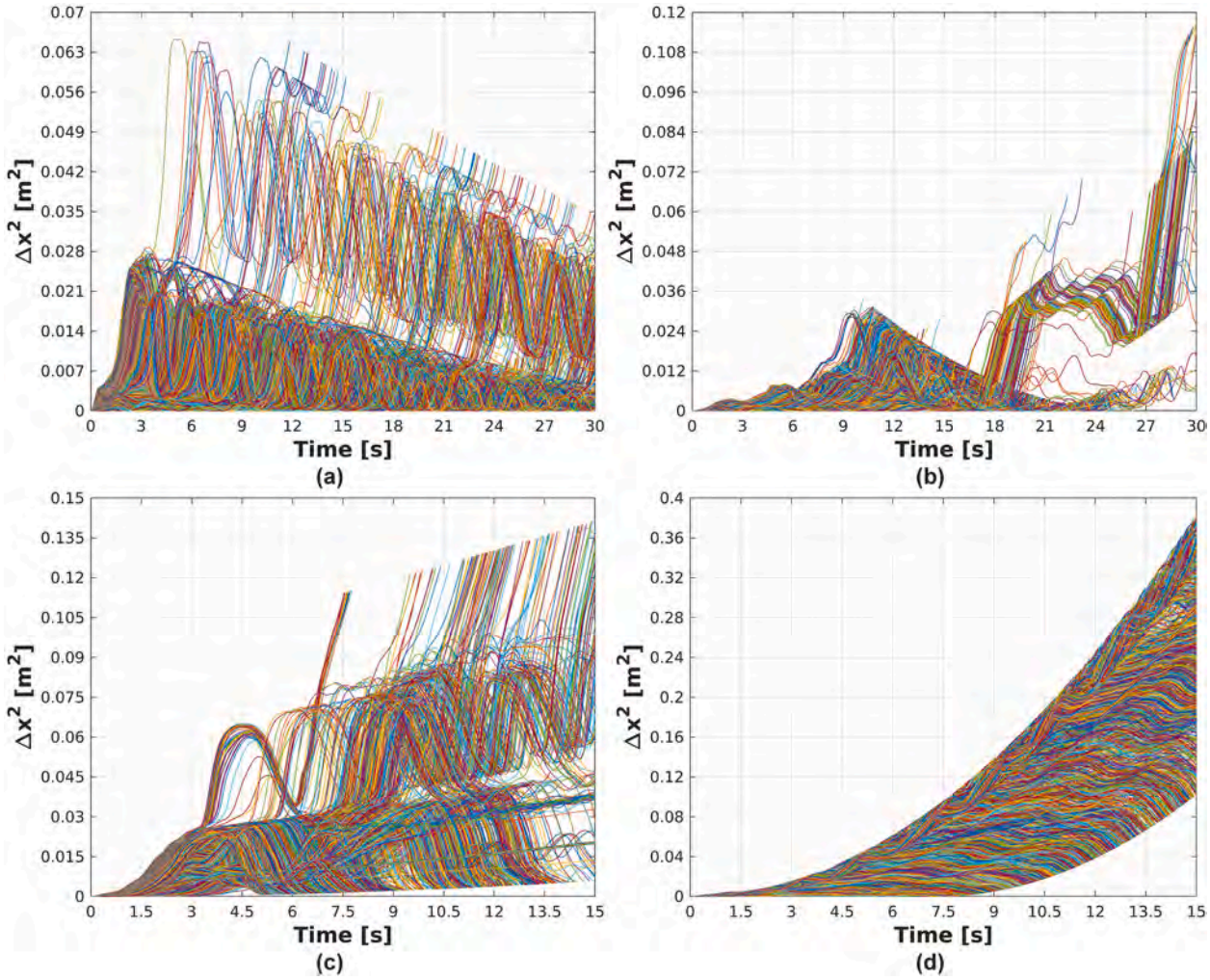

Fig. A11. Individual mean squared displacement trajectories in the streamwise (x) direction for all tracked particle pathlines in the four tested cases: (a) H=0.08 m, Q_{cz}=2.58 × 10^{-3} m^3/s; (b) H=0.08 m, Q_{cz}=1.43 × 10^{-2} m^3/s; (c) H=0.10 m, Q_{cz}=2.58 × 10^{-3} m^3/s; and (d) H=0.10, Q_{cz}=1.43 × 10^{-2} m^3/s.

Data availability

Data will be made available on request.

References

[1] K. Daizo, O. Levenspiel, Fluidization Engineering, 2nd edition, 1991. https://api.semanticscholar.org/CorpusID:93586591.
[2] P.K. Basu, Combustion and Gasification in Fluidized Beds. https://api.semanticscholar.org/CorpusID:137327942, 2006.
[3] X.B.N.E. John Grace, Essentials of Fluidization Technology, Wiley, 2020, https://doi.org/10.1002/9783527699483.
[4] K. Dewettinck, A. Huyghebaert, Fluidized bed coating in food technology, Trends Food Sci. Technol. 10 (1999) 163–168, https://doi.org/10.1016/S0924-2244(99)00041-2.
[5] D.M. Parikh, Handbook of Pharmaceutical Granulation Technology, Second edition, 2005.
[6] P. Majumder, B. Deb, R. Gupta, S.S. Sablani, A comprehensive review of fluidized bed drying: sustainable design approaches, hydrodynamic and thermodynamic performance characteristics, and product quality, Sustain. Energy Technol. Assess. 53 (2022) 102643, https://doi.org/10.1016/j.seta.2022.102643.
[7] S. Parvathaneni, B. Kodukula, M.W. Andrade, Iron-ore reduction in fluidized beds: review of commercial technologies, status, and challenges, Ind. Eng. Chem. Res. 63 (2024) 18724–18733, https://doi.org/10.1021/acs.iecr.4c02282.
[8] N. Mostoufi, J. Chaouki, Flow structure of the solids in gas-solid fluidized beds, Chem. Eng. Sci. 59 (2004) 4217–4227, https://doi.org/10.1016/j.ces.2004.06.006.
[9] S. Torfeh, R. Kouhikamali, Numerical study of different gas–solid flow regimes effects on hydrodynamics and heat transfer performance of a fluidized bed reactor, Heat Transf. Asian Res. 49 (2020) 213–235, https://doi.org/10.1002/htj.21607.
[10] Y. Li, J. Rong, K. Zhang, X. Fan, Impact of solid and gas flow patterns on solid mixing in bubbling fluidized beds, Chem. Eng. Res. Des. 132 (2018) 1037–1053, https://doi.org/10.1016/j.cherd.2017.12.014.
[11] O. Levenspiel, Tracer Technology: Modeling the Flow of Fluids. https://api.semanticscholar.org/CorpusID:92756304, 2011.
[12] Y. Wang, Z. Zou, H. Li, Q. Zhu, A new drag model for TFM simulation of gas-solid bubbling fluidized beds with Geldart-B particles, Particuology 15 (2014) 151–159, https://doi.org/10.1016/j.partic.2013.07.003.
[13] D. Gidaspow, J. Jung, R.K. Singh, Hydrodynamics of fluidization using kinetic theory: an emerging paradigm 2002 Flour-Daniel lecture, Powder Technol. (2004) 123–141, https://doi.org/10.1016/j.powtec.2004.09.025.
[14] S. Yang, K. Luo, M. Fang, J. Fan, LES-DEM investigation of the solid transportation mechanism in a 3-D bubbling fluidized bed. Part II: solid dispersion and circulation

properties, Powder Technol. 256 (2014) 395–403, https://doi.org/10.1016/j.powtec.2013.12.049.
[15] O. Levenspiel, Chemical Reaction Engineering, in: Octave Levenspiel, Third edition, 2020. https://api.semanticscholar.org/CorpusID:236909534.
[16] H.R. Norouzi, N. Mostoufi, Z. Mansourpour, R. Sotudeh-Gharebagh, J. Chaouki, Characterization of solids mixing patterns in bubbling fluidized beds, Chem. Eng. Res. Des. 89 (2011) 817–826, https://doi.org/10.1016/j.cherd.2010.10.014.
[17] D.C. Guío-Pérez, F. Johnsson, D. Pallarès, Experimental investigation of the lateral mixing of large and light particles immersed in a fluidized bed, Fuel 346 (2023), https://doi.org/10.1016/j.fuel.2023.128343.
[18] V. Verma, J.T. Padding, N.G. Deen, J.A.M. Hans Kuipers, F. Barthel, M. Bieberle, M. Wagner, U. Hampel, Bubble dynamics in a 3-D gas-solid fluidized bed using ultrafast electron beam X-ray tomography and two-fluid model, AICHE J. 60 (2014) 1632–1644, https://doi.org/10.1002/aic.14393.
[19] H. Wang, G. Qiu, J. Ye, W. Yang, Experimental study and modelling on gas–solid flow in a lab-scale fluidised bed with Wurster tube, Powder Technol. 300 (2016) 14–27, https://doi.org/10.1016/j.powtec.2016.01.025.
[20] J. Li, J.A.M. Kuipers, Effect of pressure on gas–solid flow behavior in dense gas-fluidized beds: a discrete particle simulation study, Powder Technol. 127 (2002) 173–184, https://doi.org/10.1016/S0032-5910(02)00116-X.
[21] S. Cooper, C.J. Coronella, CFD simulations of particle mixing in a binary fluidized bed, Powder Technol. (2005) 27–36, https://doi.org/10.1016/j.powtec.2004.11.041.
[22] J. Sun, Y. Zhou, C. Ren, J. Wang, Y. Yang, CFD simulation and experiments of dynamic parameters in gas-solid fluidized bed, Chem. Eng. Sci. 66 (2011) 4972–4982, https://doi.org/10.1016/j.ces.2011.06.035.
[23] K. Luo, F. Wu, S. Yang, J. Fan, CFD-DEM study of mixing and dispersion behaviors of solid phase in a bubbling fluidized bed, Powder Technol. 274 (2015) 482–493, https://doi.org/10.1016/j.powtec.2015.01.046.
[24] M. Askarishahi, M.S. Salehi, H.R. Godini, G. Wozny, CFD study on solids flow pattern and solids mixing characteristics in bubbling fluidized bed: effect of fluidization velocity and bed aspect ratio, Powder Technol. 274 (2015) 379–392, https://doi.org/10.1016/j.powtec.2015.01.025.
[25] A. Bakshi, C. Altantzis, L.R. Glicksman, A.F. Ghoniem, Gas-flow distribution in bubbling fluidized beds: CFD-based analysis and impact of operating conditions, Powder Technol. 316 (2017) 500–511, https://doi.org/10.1016/j.powtec.2017.01.005.
[26] Y. Xie, Y. Chen, Z. Fang, H. Zhou, S. Wei, L. Yang, The research of gas-solid fluidized bed bubbling behavior based on CFD-DEM coupled simulation, Chem. Eng. Res. Des. 195 (2023) 166–180, https://doi.org/10.1016/j.cherd.2023.05.053.
[27] E. Sette, D. Pallarès, F. Johnsson, Influence of bulk solids cross-flow on lateral mixing of fuel in dual fluidized beds, Fuel Process. Technol. 140 (2015) 245–251, https://doi.org/10.1016/j.fuproc.2015.09.017.
[28] M. Farha, D.C. Guío-Pérez, F. Johnsson, D. Pallarès, Characterization of the solids crossflow in a bubbling fluidized bed, Powder Technol. 443 (2024), https://doi.org/10.1016/j.powtec.2024.119967.
[29] Y. Zhang, N. Abatzoglou, S. Hudon, P.-P. Lapointe-Garant, J.-S. Simard, Dynamics of heat-sensitive pharmaceutical granules dried in a horizontal fluidized bed combined with a screw conveyor, Chem. Eng. Process. Process Intensif. 167 (2021) 108516, https://doi.org/10.1016/j.cep.2021.108516.
[30] L. Koleilat, C.K. Paasche, J. Wade, J. Hanson, C. Wassgren, P. Mort, Flow field analysis of a toroidal flow fluidized bed granulator, Chem. Eng. Res. Des. 208 (2024) 359–368, https://doi.org/10.1016/j.cherd.2024.07.003.
[31] W. Kong, B. Wang, J. Baeyens, S. Li, H. Ke, T. Tan, H. Zhang, Solids mixing in a shallow cross-flow bubbling fluidized bed, Chem. Eng. Sci. 187 (2018) 213–222, https://doi.org/10.1016/j.ces.2018.04.073.
[32] S. Migliozzi, A. Paulillo, R. Chirone, P. Salatino, R. Solimene, Hydrodynamics of compartmented fluidized beds under uneven fluidization conditions, Powder Technol. 316 (2017) 476–491, https://doi.org/10.1016/j.powtec.2016.12.052.
[33] T. Esence, H. Benoit, D. Poncin, M. Tessonneaud, G. Flamant, A shallow cross-flow fluidized-bed solar reactor for continuous calcination processes, Sol. Energy 196 (2020) 389–398, https://doi.org/10.1016/j.solener.2019.12.029.
[34] L. Hua, H. Zhao, J. Li, Q. Zhu, J. Wang, Solid residence time distribution in a cross-flow dense fluidized bed with baffles, Chem. Eng. Sci. 200 (2019) 320–335, https://doi.org/10.1016/j.ces.2019.01.054.
[35] Z. Zou, Y. Zhao, H. Zhao, L. Zhang, Z. Xie, H. Li, Q. Zhu, CFD simulation of solids residence time distribution in a multi-compartment fluidized bed, Chin. J. Chem. Eng. 25 (2017) 1706–1713, https://doi.org/10.1016/j.cjche.2017.02.010.
[36] S. Geng, Y. Qian, J. Zhan, H. Zhang, G. Xu, X. Liu, Prediction of solids residence time distribution in cross-flow bubbling fluidized bed, Powder Technol. 320 (2017) 555–564, https://doi.org/10.1016/j.powtec.2017.07.085.
[37] Z. Zou, Y. long Zhao, H. Zhao, L. bo Zhang, Z. hui Xie, H. zhong Li, Q. shan Zhu, Hydrodynamic and solids residence time distribution in a binary bubbling fluidized bed: 3D computational study coupled with the structure-based drag model, Chem. Eng. J. 321 (2017) 184–194, https://doi.org/10.1016/j.cej.2017.03.110.
[38] S. Parvathaneni, S. Karmakar, V.V. Buwa, Eulerian simulations of bubbling and jetting regimes in a fluidized bed, Particuology 75 (2023) 50–68, https://doi.org/10.1016/j.partic.2022.05.016.
[39] K. Vollmari, H. Kruggel-Emden, Numerical and experimental analysis of particle residence times in a continuously operated dual-chamber fluidized bed, Powder Technol. 338 (2018) 625–637, https://doi.org/10.1016/j.powtec.2018.07.061.
[40] Z. Jia, X. Shen, X. Lan, T. Wang, A CFD-DEM study of fluidization systems with wide particle size distributions, Chem. Eng. Sci. 318 (2025), https://doi.org/10.1016/j.ces.2025.122094.
[41] S. Kazemi, R. Zarghami, N. Mostoufi, R. Sotudeh-Gharebagh, J. Chaouki, CFD-DEM mixing of rod-like and spherical particles in fluidized beds, Powder Technol. 442 (2024), https://doi.org/10.1016/j.powtec.2024.119847.
[42] L.R. Glicksman, Scaling relationships for fluidized beds, Chem. Eng. Sci. 39 (1984) 1373–1379, https://doi.org/10.1016/0009-2509(84)80070-6.
[43] L.R. Glicksman, M. Hyre, K. Woloshun, Simplified scaling relationships for fluidized beds, Powder Technol. 77 (1993) 177–199, https://doi.org/10.1016/0032-5910(93)80055-F.
[44] P. Mirek, Influence of the model scale on hydrodynamic scaling in CFB boilers, Braz. J. Chem. Eng. 33 (2016) 885–896, https://doi.org/10.1590/0104-6632.20160334s20150348.
[45] T. Djerf, D. Pallarès, F. Johnsson, Solids flow patterns in large-scale circulating fluidised bed boilers: experimental evaluation under fluid-dynamically down-scaled conditions, Chem. Eng. Sci. 231 (2021) 116309, https://doi.org/10.1016/j.ces.2020.116309.
[46] J. Ding, D. Gidaspow, A bubbling fluidization model using kinetic theory of granular flow, AICHE J. 36 (1990) 523–538, https://doi.org/10.1002/aic.690360404.
[47] R. Jackson, M.D. Shattuck, The dynamics of fluidized particles. https://api.semanticscholar.org/CorpusID:121740919, 2000.
[48] S. Yuu, H. Nishikawa, T. Umekage, Numerical Simulation of Air and Particle Motions in Group-B Particle Turbulent Fluidized Bed. www.elsevier.comrlocaterpowtec, 2001.
[49] N. Xie, F. Battaglia, S. Pannala, Effects of using two- versus three-dimensional computational modeling of fluidized beds. Part I, hydrodynamics, Powder Technol. 182 (2008) 1–13, https://doi.org/10.1016/j.powtec.2007.07.005.
[50] B. Lu, W. Wang, J. Li, Searching for a mesh-independent sub-grid model for CFD simulation of gas-solid riser flows, Chem. Eng. Sci. 64 (2009) 3437–3447, https://doi.org/10.1016/j.ces.2009.04.024.
[51] V. Jiradilok, D. Gidaspow, S. Damronglerd, W.J. Koves, R. Mostofi, Kinetic theory based CFD simulation of turbulent fluidization of FCC particles in a riser, Chem. Eng. Sci. 61 (2006) 5544–5559, https://doi.org/10.1016/j.ces.2006.04.006.
[52] D. Gidaspow, R. Bezburuah, J. Ding, Hydrodynamics of circulating fluidized beds: kinetic theory approach, Dept. of Chemical …, Illinois Inst. of Tech., Chicago, IL (United States), 1991.
[53] M. Syamlal, W. Rogers, T.J. OBrien, MFIX Documentation Theory Guide, USDOE Morgantown Energy Technology Center (METC), WV (United States), 1993.
[54] D. Gidaspow, Multiphase Flow and Fluidization: Continuum and Kinetic Theory Descriptions, Academic Press, 1994.
[55] H. Arastoopour, D. Gidaspow, E. Abbasi, Conservation and constitutive equations for fluid–particle flow systems, in: Computational Transport Phenomena of Fluid-particle Systems, Springer, 2016, pp. 9–44.
[56] M. Syamlal, Multiphase Hydrodynamics Of Gas-Solids Flow (Multiphase, Two Phase, Hydrodynamics), Illinois Institute of Technology, 1985.
[57] H. Arastoopour, D. Gidaspow, E. Abbasi, Computational Transport Phenomena of Fluid-Particle Systems, Springer, 2017.
[58] W.-C. Yang, Handbook of Fluidization and Fluid-particle Systems, CRC press, 2003.
[59] D. Pallares, P.A. Díez, F. Johnsson, Experimental analysis of fuel mixing patterns in a fluidized bed, 2007.
[60] E. Sette, D. Pallarès, F. Johnsson, F. Ahrentorp, A. Ericsson, C. Johansson, Magnetic tracer-particle tracking in a fluid dynamically down-scaled bubbling fluidized bed, Fuel Process. Technol. 138 (2015) 368–377.
[61] A. Köhler, E. Cano-Pleite, A. Soria-Verdugo, D. Pallarès, F. Johnsson, Modeling the motion of fuel particles in a fluidized bed, Fuel 305 (2021) 121424, https://doi.org/10.1016/j.fuel.2021.121424.
[62] V. Jiradilok, D. Gidaspow, R.W. Breault, Computation of gas and solid dispersion coefficients in turbulent risers and bubbling beds, Chem. Eng. Sci. 62 (2007) 3397–3409, https://doi.org/10.1016/j.ces.2007.01.084.
[63] A. Einstein, Investigations on the Theory of the Brownian Movement, Courier Corporation, 1956.
[64] S. Yang, K. Luo, K. Qiu, M. Fang, J. Fan, Coupled computational fluid dynamics and discrete element method study of the solid dispersion behavior in an internally circulating fluidized bed, Ind. Eng. Chem. Res. 53 (2014) 6759–6772, https://doi.org/10.1021/ie4041725.
[65] G. Lian, W. Zhong, X. Liu, CFD-DEM investigation of fuel dispersion behaviors in a 3D fluidized bed, Ind. Eng. Chem. Res. 60 (2021) 13272–13285, https://doi.org/10.1021/acs.iecr.1c02443.
[66] N. Mostoufi, J. Chaouki, Local solid mixing in gas–solid fluidized beds, Powder Technol. 114 (2001) 23–31, https://doi.org/10.1016/S0032-5910(00)00258-8.
[67] D. Liu, X. Chen, Lateral solids dispersion coefficient in large-scale fluidized beds, Combust. Flame 157 (2010) 2116–2124, https://doi.org/10.1016/j.combustflame.2010.04.020.
[68] J. Jung, D. Gidaspow, I.K. Gamwo, Measurement of two kinds of granular temperatures, stresses, and dispersion in bubbling beds, Ind. Eng. Chem. Res. 44 (2005) 1329–1341, https://doi.org/10.1021/ie0496838.
[69] B. Chalermsinsuwan, D. Gidaspow, P. Piumsomboon, Two- and three-dimensional CFD modeling of Geldart A particles in a thin bubbling fluidized bed: comparison of turbulence and dispersion coefficients, Chem. Eng. J. 171 (2011) 301–313, https://doi.org/10.1016/j.cej.2011.04.007.
[70] T. Samruamphianskun, P. Piumsomboon, B. Chalermsinsuwan, Computation of system turbulences and dispersion coefficients in circulating fluidized bed downer using CFD simulation, Chem. Eng. Res. Des. 90 (2012) 2164–2178, https://doi.org/10.1016/j.cherd.2012.06.009.
[71] M. Kashyap, B. Chalermsinsuwan, D. Gidaspow, Measuring turbulence in a circulating fluidized bed using PIV techniques, Particuology 9 (2011) 572–588, https://doi.org/10.1016/j.partic.2011.06.007.

[72] B. Chalermsinsuwan, P. Piumsomboon, D. Gidaspow, Kinetic theory based computation of PSRI riser: part I-estimate of mass transfer coefficient, Chem. Eng. Sci. 64 (2009) 1195–1211, https://doi.org/10.1016/j.ces.2008.11.010.
[73] M. Farha, D.C. Guío-Pérez, J. Aronsson, F. Johnsson, D. Pallarès, Assessment of experimental methods for measurements of the horizontal flow of fluidized solids under bubbling conditions, Fuel 348 (2023), https://doi.org/10.1016/j.fuel.2023.128515.
[74] K. Jang, Y. Feng, H. Li, Investigation of bubble behavior in gas-solid fluidized beds with different gas distributors, Chem. Eng. Technol. 44 (2021) 723–731, https://doi.org/10.1002/ceat.202000156.
[75] N.F. Nthatisi, A.F. Van Der Merwe, Computational Fluid Dynamics (CFD) modelling of the effect of distributor plate geometry in the bubbling fluidized bed reactor, S. Afr. J. Chem. Eng. 43 (2023) 46–59, https://doi.org/10.1016/j.sajce.2022.09.010.
[76] G. Gustafsson, G.M. Castilla, D. Pallarès, H. Ström, Effective lateral dispersion of momentum, heat and mass in bubbling fluidized beds, Front. Chem. Sci. Eng. 18 (2024) 151, https://doi.org/10.1007/s11705-024-2503-4.
[77] H. Zhang, Y. Huang, X. An, A. Yu, J. Xie, Numerical prediction on the minimum fluidization velocity of a supercritical water fluidized bed reactor: effect of particle size distributions, Powder Technol. 389 (2021) 119–130, https://doi.org/10.1016/j.powtec.2021.05.015.
[78] W. Long, J. Ji, W. Zeng, Z. Han, H. Zhang, X. An, S. Jiang, CFD-DEM investigation on effects of particle size distribution and gas temperature on minimum fluidization velocity of pyrites, Particuology 96 (2025) 244–255, https://doi.org/10.1016/j.partic.2024.11.009.
[79] V. Mathiesen, T. Solberg, B.H. Hjertager, Predictions of gas/particle flow with an Eulerian model including a realistic particle size distribution, Powder Technol. 112 (2000) 34–45.
[80] S.A. Jayarathna, C.K. Jayarathna, W.J. Wu, B.M. Halvorsen, Influence of particle size distributions on CFD simulations and experiments of bubbling fluidized beds, in: AIChE Annual Meeting 2008, 2008, pp. 16–21.
[81] J. Chandler, H. Obermaier, K.I. Joy, Interpolation-based pathline tracing in particle-based flow visualization, IEEE Trans. Vis. Comput. Graph. 21 (2014) 68–80.
[82] M. Farha, D.C. Guío-Pérez, F. Johnsson, D. Pallarès, Frictional losses in a bubbling fluidized bed with horizontal flow of solids, Int. J. Multiphase Flow (2025) 105192, https://doi.org/10.1016/j.ijmultiphaseflow.2025.105192.
[83] M. Upadhyay, A. Kim, H. Kim, D. Lim, H. Lim, An assessment of drag models in eulerian–eulerian cfd simulation of gas–solid flow hydrodynamics in circulating fluidized bed riser, ChemEngineering 4 (2020) 37.
[84] R. Khezri, W.A.W.A.K. Ghani, S.M. Soltani, D.R.A. Biak, R. Yunus, K. Silas, M. Shahbaz, S.R. Motlagh, Computational fluid dynamics simulation of gas–solid hydrodynamics in a bubbling fluidized-bed reactor: effects of air distributor, viscous and drag models, Processes 7 (2019) 1–16, https://doi.org/10.3390/pr7080524.
[85] T. Hirama, M. Ishida, T. Shirai, The lateral dispersion of solid particles in fluidized beds, Kagaku Kogaku Ronbunshu 1 (1975) 272–276.
[86] Y.F. Shi, M.X. Gu, Lateral mixing of solids in fluidized beds with partitions, in: World Congress III of Chemical Engineering, Tokyo, Japan, 1986, pp. 465–468.
[87] G. Martinez Castilla, A. Larsson, L. Lundberg, F. Johnsson, D. Pallarès, A novel experimental method for determining lateral mixing of solids in fluidized beds – quantification of the splash-zone contribution, Powder Technol. 370 (2020) 96–103, https://doi.org/10.1016/j.powtec.2020.05.036.
[88] E. Sette, D. Pallarès, F. Johnsson, Experimental evaluation of lateral mixing of bulk solids in a fluid-dynamically down-scaled bubbling fluidized bed, Powder Technol. 263 (2014) 74–80, https://doi.org/10.1016/j.powtec.2014.04.091.